Solidification furnace for in situ observation of bulk transparent systems and image analysis methods

F L Mota, M Medjkoune, L Strutzenberg Littles, A Karma, N Bergeon

Solidification furnace for in situ observation of bulk transparent systems and image analysis methods

F.L. Mota,[1] M. Medjkoune,[1] L. Strutzenberg Littles,[2] A. Karma,[3] and N. Bergeon[1]
[1)]*Aix Marseille Univ, Université de Toulon, CNRS, IM2NP, Marseille, France*
[2)]*Marshall Space Flight Center, Huntsville, USA*
[3)]*Department of Physics and Center for Interdisciplinary Research on Complex Systems, Northeastern University, Boston, USA*

(*Electronic mail: fatima.lisboa-mota@im2np.fr)

(Dated: 25 May 2023)

This paper aims to describe the experimental framework of the Directional Solidification Insert (DSI), installed onboard the International Space Station (ISS), dedicated to the in situ and real-time characterization of the dynamic selection of the solid-liquid interface morphology in bulk samples of transparent materials under diffusive growth conditions. The in situ observation of the solid-liquid interface is an invaluable tool for gaining knowledge on the time-evolution of the interface pattern because the initial morphological instability evolves nonlinearly and undergoes a reorganization process. The result of each experiment, characterized by the sample concentration, a thermal gradient and a pulling rate, is a large number of images. Interpretation of these images necessitates a robust identification of each cell/dendrite position and size during the entire solidification. Several image analysis methods have been developed to achieve this goal reliably despite varying contrast and noise levels, and are described in details. Typical solidification experiments are presented and the dynamics of the pattern formation are analyzed to illustrate the application of the image analysis methods.

I. INTRODUCTION

It is well known that materials properties are largely controlled by the microstructure left in the solid during processing, so that the precise mastering of its development during solidification is essential to reproducibly tailor products of specified quality. It is therefore necessary to unceasingly deepen the quantitative understanding of the basic physical principles governing microstructure formation, from the microscopic to the macroscopic scales. The properties and the reliability of materials processed by solidification techniques, such as continuous casting or laser welding, are governed by the microstructural characteristics of cells and dendrites.

Pattern formation is important in several fields of sciences, and the process of pattern selection is quite complex because it occurs in a highly non-linear growth regime[1]. The interface between the solid and the liquid exhibits complex patterns during the directional solidification of alloys, which are analogous to patterns that form in other fields such as combustion, fluid dynamics, geology and biology. Solidification patterns in three dimensions can be accurately studied through directional solidification experiments, and an understanding of solidification patterns will provide a general theoretical framework for a broader problem of pattern formation in nature. The evolution of these patterns proceeds under dynamic conditions, in which they self-organize into a rather periodic array. The pattern is characterized in terms of primary spacing and order/disorder level, with the stationary pattern being reached when the primary spacing no longer changes. In situ and real-time observation of the solid-liquid interface is an important tool for studying the time evolution of the interface. In light of this, transparent organic analogs have been extensively used. They behave like metallic alloys regarding solidification but are transparent to visible light so that optical techniques are sufficient for their observation[2,3].

The strong influence of convection on the solidification interface is a critical impediment to the study of three-dimensional (3D) pattern evolution in ground-based experiments. Extensive ground-based studies carried out in metallic and organic bulk samples have clearly established that fluid flow modifies the solute boundary layer, influencing the pattern development[4–6].

Directional solidification experiments under low gravity conditions provide a unique framework for investigating microstructure development in spatially extended sample geometries, with negligible convection effects and under well-controlled conditions of growth rate, temperature gradient, and alloy composition[7–9]. The Directional Solidification Insert (DSI) is dedicated to in situ and real-time characterization of the dynamical selection of the solid-liquid interface morphology in bulk samples of transparent materials. It was developed by the French Space Agency (CNES) in the frame of the DEvice for the study of Critical LIquids and Crystallization (DECLIC) project. The DECLIC facility of CNES was launched for the first time with a STS-128 shuttle flight (August 2009) as part of a joint NASA/CNES research program and was installed on the International Space Station (ISS) in a microgravity environment. The main instrument monitoring is performed from the CADMOS, which is the CNES center for the development of microgravity activities and space operations (Toulouse, France). Taking advantage of provided tele-science capabilities, scientists have the ability to follow and remotely control experiments.

The DECLIC facility is a compact, multi-user facility for conducting experiments in the fields of fluid physics and materials science, and more generally on transparent media, within the ISS environment. Figure 1a shows the DECLIC payload fitted in the EXPRESS RACK 4 of the ISS. The two DECLIC lockers are located in the top right quarter of the rack. The electronic locker, at the bottom, is common to all experiments

and mainly contains electronics and some optical resources. Different inserts that contain elements specific to each topic complete the facility (experimental locker at the top), and DSI is one of them (Figure 1b). The DSI was commissioned in December 2009, and 51 solidification experiments over six runs of three weeks each were performed from April 2010 to April 2011. The DSI was then brought back to ground to perform experiments with control parameters similar to those used in microgravity so that convection influence could be addressed[6,10]. After a sample change, a second flight campaign (DSI-R) was performed with 50 experiments during six runs from October 2017 to November 2018 plus two additional runs in 2022.

In addition to yielding new insights into solidification microstructures, the DECLIC-DSI experiments are a major contribution to the formation of a benchmark database necessary for the calibration and validation of numerical simulations. For example, the DSI experiments analysis revealed the complex thermal field evolution in bulk samples and its consequences on solidification patterns[11], thus leading to the development of a phase field coupled with thermal calculations to improve simulation accuracy[12]. Experiments especially highlighted the major influence of interface curvature, subboundaries and pattern misorientations which are unavoidable in 3D growth, thus supporting numerical simulations to include such defects[13,14]. Experiments performed on DECLIC-DSI also led to unprecedented observations that have been analyzed with the support of 3D phase-field numerical simulations. For example, regarding grain structure, it was evidenced that individual cells from one grain can unexpectedly invade a nearby grain of different misorientation, either as a solitary cell or as rows of cells[15]. This invasion process causes grains to interpenetrate each other and hence grain boundaries to adopt highly convoluted shapes, thereby potentially impacting mechanical behavior and other properties. Also, unprecedented observations of breathing-mode oscillations in spatially extended cellular arrays have been performed and widely analyzed, experimentally and numerically[16–20].

The result of each experiment performed in DECLIC-DSI is a large number of images that must be analyzed to quantitatively characterize the cellular or dendritic pattern and its time evolution. The method of data treatments that had to be developed to tackle these image sequences will be described in this article. The experimental framework is introduced in Section II. Specific image procedures and algorithms that have to be developed to systematically analyze the experimental data in spite of their variability are presented in Section III. Analyses are conducted on typical experiments and described in Section IV.

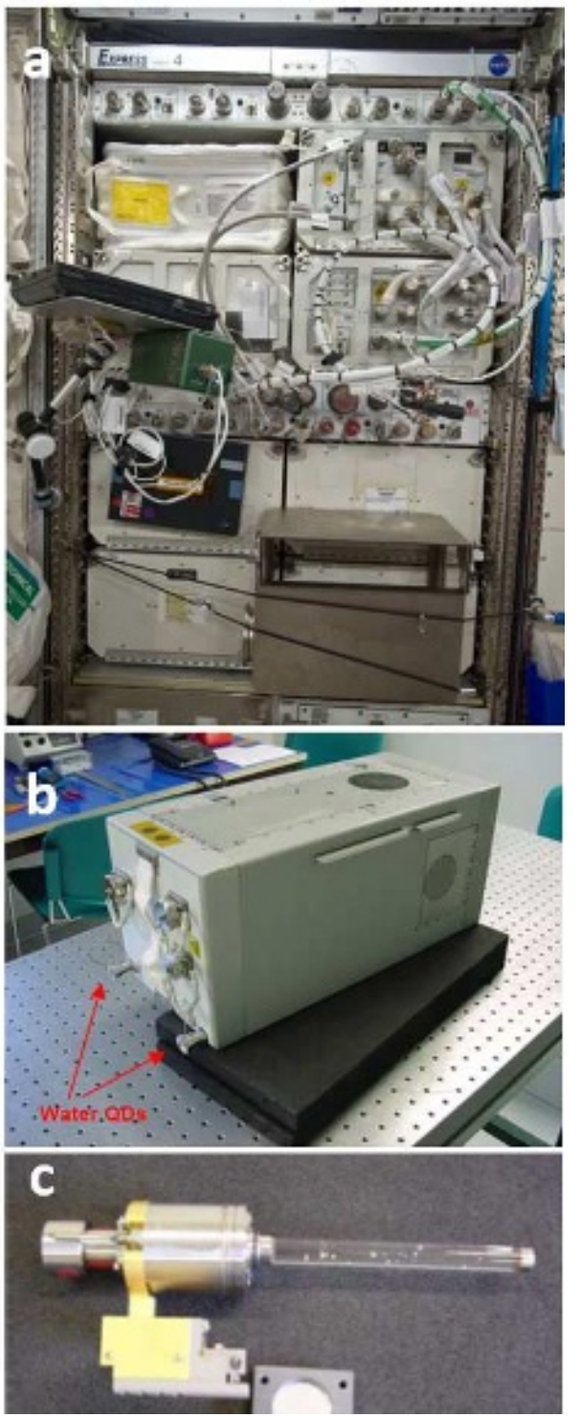

FIG. 1. (a) DECLIC facility installed onboard ISS. The experimental and electronic DECLIC lockers are located in the top right quarter of the rack. (b) Flight Model of the DSI insert that can be hosted in the experimental locker (at the top). (c) The DSI cartridge with the quartz tube containing the alloy (left), the compensator and motorization arm (right).

II. EXPERIMENTAL FRAMEWORK

Essentially, the DECLIC-DSI insert consists of two elements: the Bridgman furnace and the experimental cartridge (see Figure 2). The Bridgman furnace allows the directional solidification of the alloy, characterized by its solute concentration C_0, by pulling it at constant pulling rate V within a ther-

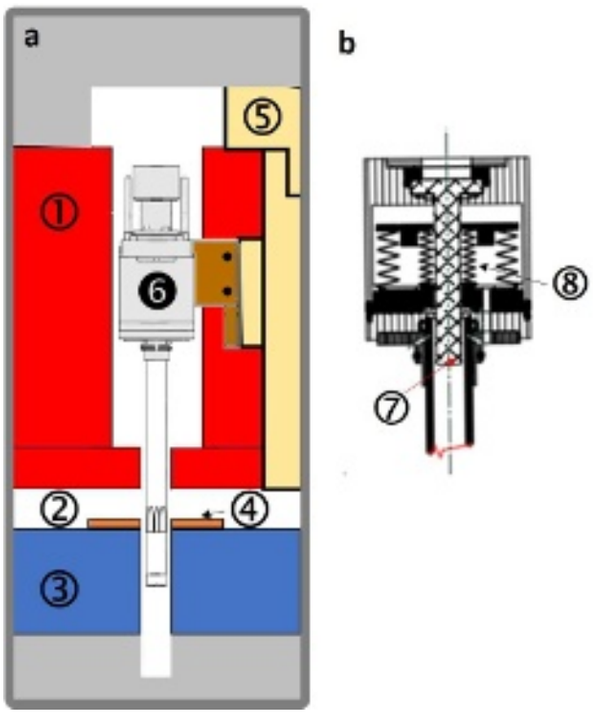

FIG. 2. (a) Schematic drawing of the directional solidification furnace where: ① is the hot zone, ② the median (non–regulated) zone, ③ the cold zone, ④ the booster heater, ⑤ the motorization and ⑥ the cartridge. (b) Transverse cut of the volume compensator region of the cartridge where one can distinguish ⑦ the immersed lens and ⑧ the bellows to accommodate volume variations.

mal gradient G. Considering a given alloy concentration, fixing the thermal gradient G, one can set the pulling rate to create various interface morphologies, ranging from planar front to cellular and finally dendritic patterns.

The experimental cartridge containing the alloy, showed in Figure 1c, includes a quartz crucible and a system of volume compensation made of stainless steel that is useful to accommodate the sample volume variations associated with phase changes (see schema in Figure 2b). The cylindrical crucible has an inner diameter of 10 mm and enables a solidification length of 100 mm, allowing the study of the entire development of extended 3D patterns, from the initial stage to the steady-state. Thanks to the complete axial transparency of the crucible, the solid-liquid interface can be observed by three different optical modes (Figure 3). The primary, and most frequently used, mode is the top-view (axial) observation (Figure 3a). The crucible is illuminated from the bottom and the interface is observed from the top. With this optical diagnostic, a light-emitting diode (LED) placed close to the cartridge end, on the cold side, is used for Wide Field of View (WFOV) and Narrow Field of View (NFOV). One of the optical challenges of such observation during solidification comes from the progressive decrease of the liquid thickness in favor of the solid one, meaning that the interface position inside the crucible keeps moving over a long distance. An afocal relay including a 6.9 mm diameter lens immersed in the liquid phase was implemented in order to maintain a constant position of the solidification front intermediate image (details on the conception of this optical system are given elsewhere[21]). The whole cartridge along its main axis is also part of the object beam of a Mach-Zehnder interferometer that enables determining the shape of the front by taking advantage of the refraction index difference between the liquid and solid phases (Figure 3b)[16,22,23]. Another optical challenge was the observation of the solidification front perpendicularly to the cartridge axis through the cylindrical crucible (side-view observation of the interface). With this transverse diagnostic, a LED is used as light source and a cylindrical custom made lens is accommodated in the non-regulated zone of the insert around the cartridge (Figure 3c).

The hot and cold zones of the Bridgman furnace, respectively ① and ③ in Figure 2a, are set up in a way to impose a thermal gradient ranging from 10 to 30 K/cm and to maintain the solid-liquid interface in the non-regulated area located between the cold and hot zones (② in the schematic drawing of Figure 2a). The set temperature for the hot zone ranges from ambient up to 160C, and for the cold zone from ambient down to -30C. The non-regulated zone also includes a booster heater able to locally inject power, from 0 to 7 W, into the crucible (④ in Figure 2a). This is used to flatten the solidification front shape that is usually curved due to isotherm's shape and to latent heat evacuation during solidification[24].

No direct in situ measurement of the thermal gradient is available in the DSI as no thermocouple is inserted inside the sample to avoid thermal perturbations. Control temperatures are imposed to the regulating areas but these areas do not touch the cartridge as a gap of 1 mm was necessary for cartridge manipulations. These elements, added to the cylindrical geometry and the difference of conductivity between the quartz crucible and the alloy, lead to a thermal field that is difficult to characterize analytically. Two different sets of temperatures have been used, associated to two different values of the thermal gradient, G_1 and G_2. Experimental determinations of the thermal gradients at the interface, at rest ($V = 0$), were performed during DSI-R experiments. The displacement of the interface Δz associated to a small shift ΔT of the control temperatures of hot and cold areas, and of the booster heater, was measured. Assuming that the gradient is constant in the area over the interface displacement distance, the thermal gradient is then simply $\frac{\Delta T}{\Delta z}$. A temperature shift of 2C led to the measures G_1 = (20.7 $\pm$ 0.8) K/cm and G_2 = (12.5 $\pm$ 0.3) K/cm. The complete thermal analysis of the furnace is performed using CrysVUn®/ CrysMAS ®software, which was designed for the global modeling of solidification processes[25,26]. Calculations are based on a method of finite volumes on unstructured grids that includes a geometrical model of the furnace, crucible and sample and assignment of the relevant physical properties to all materials involved in this setup. The temperatures applied to the different elements of the furnace, pulling rates and sample composition are entered as input parameters for the numerical simulations. These calculations yielded G_1 = 19 K/cm and G_2 = 11 K/cm, which are consistent with experimentally determined gradients.

The crucible is pulled down from the hot zone into the cold

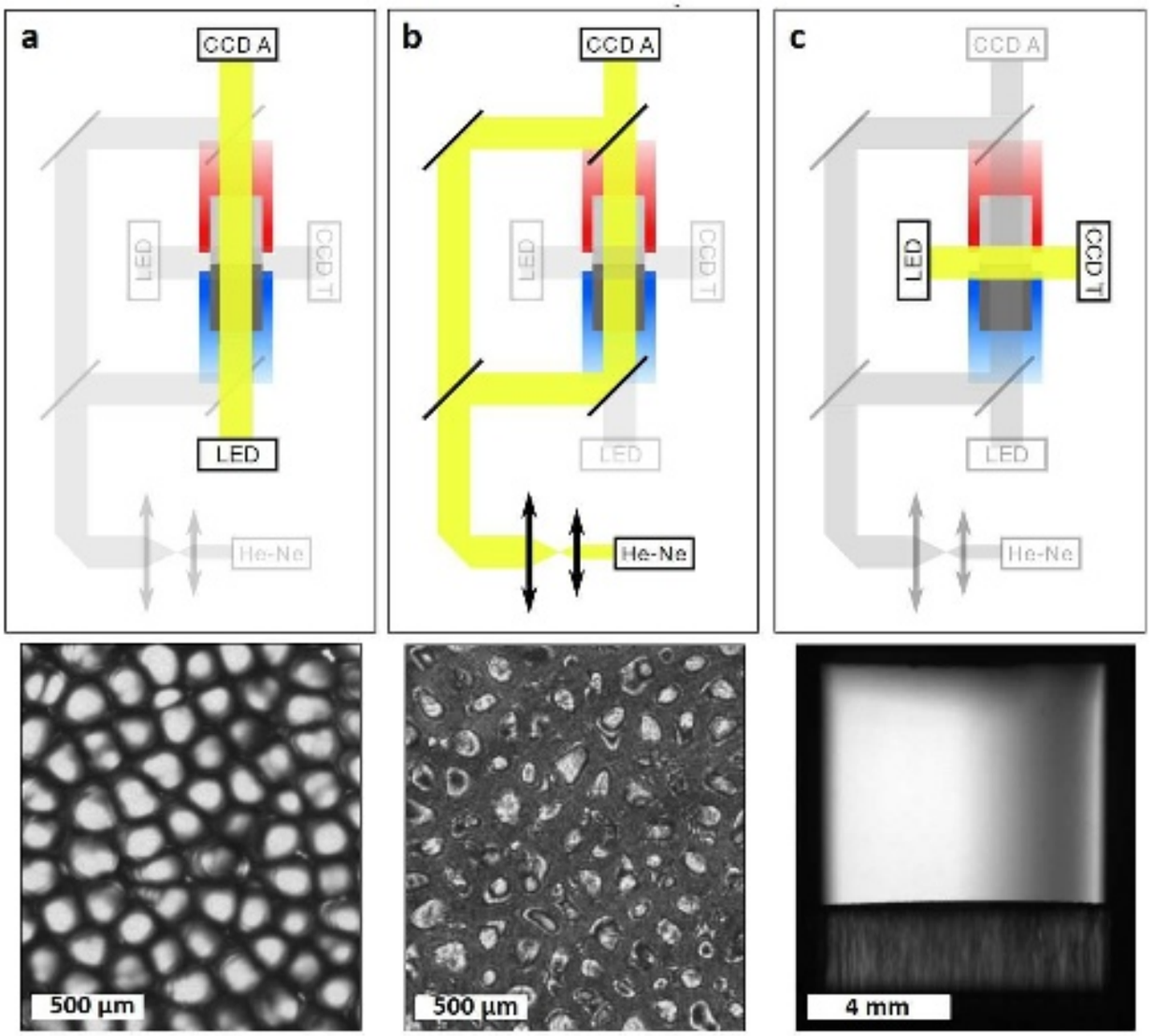

FIG. 3. Schematic representation of the optical acquisition in DECLIC-DSI (top) and the corresponding raw images (bottom): (a) axial direct; (b) axial interferometric; and (c) transverse direct. The red and blue rectangles represent, respectively, the hot and cold zones of the Bridgman furnace. The labels A and T denote axial and transverse views of the sample, respectively. The yellow regions represent the light path, rather white in (a) and (c), or a laser beam in (b).

zone during the experiment, at a rate ranging from 0.1 to 30 m/s, with 1% stability over a 100 mm travel (the motorization is schematically represented in Figure 2a by ⑤). The optical resolution in the object plane for the DSI-Flight Model insert was measured as follows: axial direct and interferometry WFOV, 7.1 m within a FOV of ⌀ 7.3 mm ; axial direct NFOV, 3.1 m within a FOV of ⌀ 3.1 mm; transverse WFOV, 13.5 m within a FOV of ⌀ 8.1 mm; transverse NFOV, 1.1 m within a FOV of ⌀ 1.15 mm. In axial imagery the focusing capability on the solidification front is -10 to +30 mm (centered in middle of the non-regulated zone); in transverse imagery the focusing capability on the media, plane of cartridge is -2.5 to +2.5 mm.

The cartridge is filled under vacuum with a succinonitrile (SCN) – camphor alloy, typically using SCN purified through distillation and zone melting. Once sealed, the cartridge is inserted into the Bridgman furnace of a laboratory device with characteristics similar to the DSI-Flight Model. A monocrystalline seed with a direction $< 100 >$ parallel to the pulling axis is prepared on ground and kept unmelted during all the experimental campaigns. The booster heater is a very useful tool to prepare this well-oriented single crystal. The sample is first completely melted, and then a very thin polycrystalline solid seed is realized by pulling. Increasing the booster heater temperature, all the small grains formed at the borders of the crucible are melted radially , and only the central one remains (Figure 4a). By decreasing the booster heater temperature, this last grain is then expanded laterally until it fills the whole

section of the sample (Figure 4b). In order to check the orientation of this single crystal, a high pulling rate is applied to obtain dendritic patterns. In the case of dendrites, the growth direction is strongly influenced by the crystal orientation, and dendrites grow along $< 100 >$ directions in the cubic system (as succinonitrile). If the single crystal orientation is not correct, i.e. dendrite growth direction not parallel enough to the observation axis, the whole solid seed is remelted and the procedure is repeated until success. Figure 4 shows the result of a procedure that was a success with the good orientation (Figure 4c).

III. IMAGE TREATMENT METHODS FOR MICROSTRUCTURE ANALYSIS

Top-view (axial) observation is the main tool to observe cellular and dendritic pattern formation and evolution, and to quantitatively characterize these patterns. This paper will be focused on this top-view optical diagnostic and present the different methods developed to analyze raw images. Examples and methods of analyses conducted with the transverse[11,27] and interferometry[19,22,23] diagnostics will not be detailed in this paper.

The cell or dendrite tips advance during solidification leaving long irregular columns in the solid behind. These columns can be thought of as light waveguides when illuminated from the crucible bottom. Parts of the tip surface that are more normal to the optical axis generally appear brighter, while the grooves between cells or dendrites, which are farther from the normal, appear darker. Seen from the top, a 2D pattern is obtained that keeps evolving during the whole solidification.

The resulting raw data are a sequence of images of the interface during the whole solidification, from the onset of morphological instability to the stationary pattern. Including all diagnostics, several thousand images are produced during each solidification. The amount of raw data affords an extremely rich analysis of the phenomena at the interface but this implies accurately interpreting the structure conveyed in vast quantities of images. The analysis of axial images requires several steps. First, an algorithm for local contrast enhancement is applied to each image, which uses histograms computed over different tile regions of the image. Local details can therefore be enhanced even in regions that are darker or lighter than most of the image. Then, a binary mask is created to label each structure separately, and to calculate its center position. The corresponding procedures will be explained in the next subsections. A Voronoi tessellation is then applied to these points. All triple and quadruple intersections are detected and removed so that only a figure of segments remains. Each segment corresponds to a boundary between two cells/dendrites so that counting the number of segments attached to one structure gives the number of first neighbors. Segments linking adjacent cells or dendrites are measured so that the primary spacing (i.e., the mean distance between a tip's center and the centers of its first neighbors) can be measured for the whole pattern . The labels of each cell or dendrite are associated across images so that it can be followed through the successive images, and its creation, movement, and elimination characterized, as well as the sidebranching development in the case of dendrites. The tracking algorithm will be described in Section III F.

When treating axial images, the identification of each cell or dendrite is important, since an error in detection of one of them affects the primary spacing measurement of all its neighbors, and erroneous identification of a cell or dendrite in one image can disrupt its cross-image labeling. Moreover, the microstructure that emerges during solidification form a complex optical system that introduces unpredictable brightness variations, such as bright spots between dendrites, and areas of various contrasts. Considering the very large number of images, each containing hundreds of cells or dendrites, a reliable treatment that is automated as much as possible is necessary.

Over time, many image analysis procedures have been developed to treat real-time bulk transparent alloy images effectively and to adapt to different problems. The first procedures were developed on both analySIS and Visilog software to facilitate exploitation of results[27]. For the last few years, these procedures evolved and image binarization methods were conceived and developed making extensive use of Python programming language libraries[28,29], first for cellular microstructures and then updated for dendritic patterns. These procedures will be described in the next subsections.

A. Cell centers identification by multi-threshold masking

Even after a local equalization rank filter[28], the vast majority of images have features that cannot be binarized by a single threshold value. The median of pixel brightness (50^{th} centile) of the equalized image has been found to be a reliable threshold value in the sense that the apparent cell surface is adequately estimated by the mask. But, especially during the early stages of solidification, this value is too low for segmentation. The newly formed cells, or the brightness irregularities between cells, create bright areas that are above the threshold, erroneously joining several cells. In contrast, the 75^{th} centile has been found to be a sufficiently high threshold value in the sense that very few cells are erroneously joined, but the cell surfaces are underestimated, resulting in often erroneous center identification, or in some cases entirely omitted cells.

A simple solution that has worked well on images of the early stages of solidification, provided that the overall contrast is sufficient, is a dual-threshold and watershed strategy. Two masks Mm and Mq are produced by thresholding the image at its 50^{th} and 75^{th} centile levels. Each region of white pixels in Mq is given a distinct arbitrary label. These labels are superposed onto the Mm mask, and propagated by a watershed procedure[28]. The result is a mask where the cell surfaces are accurately identified, and, even when the identified cell surfaces touch, each cell has a unique label from which the cell surface center can be trivially calculated.

This strategy reliably separates all visible surfaces, even when the interface presents many irregular features. As a comparison, Figure 5a shows the centers and segmentation that are produced from a classic threshold method, incorrectly

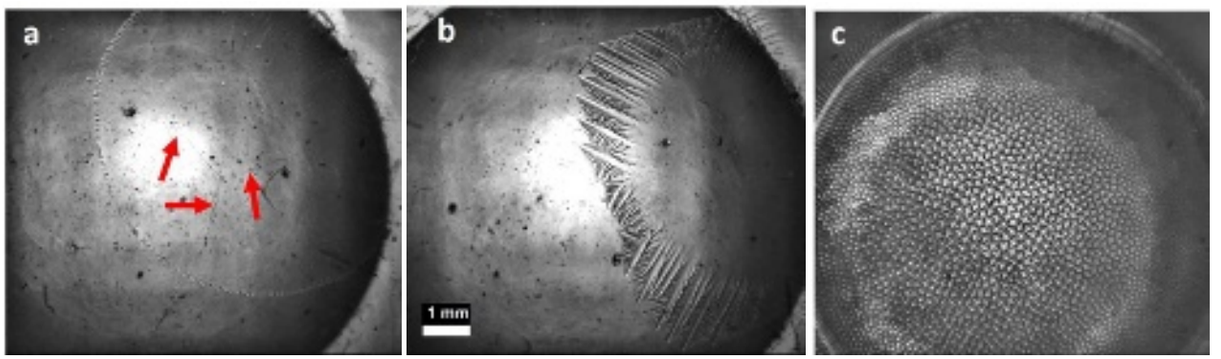

FIG. 4. Solid seed fabrication on ground (in laboratory device) for a SCN–0.46 % wt camphor alloy: (a) melting of the very thin polycrystalline solid seed (the red arrows indicate some grain boundaries); (b) expansion of the last single crystal grain; (c) test of the crystal orientation by pulling.

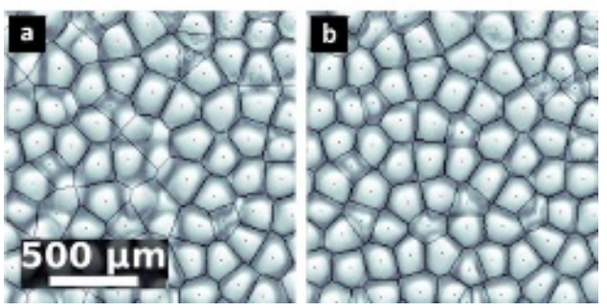

FIG. 5. Comparison between the cell's center determination using (a) classical binarization methods and (b) the multi-threshold masking method.

identifying the cell topology, and Figure 5b shows the same image after application of the multi-threshold method which gives clearly better results.

B. Cell centers identification by concentric features

The areas near the crucible walls exhibit low contrast during the late stages of solidification of some experiments, due to the long pulled distance (Figure 6a). The previously discussed equalization results in high noise, and large regions of untreatable data. It is common, however, that many new cells nucleate in these regions, so their analysis is important to the study of primary spacing evolution. The method that will be described in the following is successfully used to reliably find the centers of cells under extremely low signal to noise ratio, where, even after manual equalization, the human eye has trouble distinguishing the cells. This method works by taking advantage of the hypothesis that the features of the 2D projection of a cell are generally concentric. A cell center will be surrounded by relatively many roughly concentric features (differences in pixel brightness where the direction of greatest brightness change points towards or away from the center), regardless of the magnitude of these features.

To partially normalize the image dynamic range, the algorithm first produces a Gaussian blur of the image, and divides the value of each pixel in the original by the value of the corresponding pixel in the blurred image (Figure 6b). The edges are exaggerated by applying a second order Gaussian derivative Laplace filter and a gradient magnitude filter (Figure 6c)[28]. The result is effectively a map of level curves that are perpendicular to the directions of greatest change of brightness, even for areas of the image of extremely low contrast.

A Sobel filter is applied to find the gradient (Figure 6d). A separate image is created with the values of all the pixels initially set to zero. This image will be used as a ledger. One iterates over each pixel in the Sobel image, and adds a constant arbitrarily predefined value to each ledger pixel that lies in a 50-pixel straight line in the Sobel direction, centered at the Sobel pixel. The result is a ledger image, where pixel brightness is higher when it is in the neighborhood and direction of many changes in intensity, regardless of the magnitude of these changes (Figure 6e). The position of cell centers, i.e. the place where many concentric features are centered, is then determined by finding the local maxima in this ledger image. Figure 6f shows the identification of centers superimposed to the initial raw image to demonstrate the efficiency of this procedure in regions of poor contrast.

C. Dendrite centers identification by threshold masking

Threshold masking is a simple method to detect center for non-concentric structures, such as dendrites. To detect dendrites centers, the first step is to detect the groove between the dendrites. The raw image is binarized using a threshold value below which the groove is considered. This threshold must be high enough to isolate each dendrite from each other (Figure 7a). Then a second threshold is applied that takes into account the minimal size that an object must have to be counted as a new center.

The combination of both images reliably separates all visible surfaces, even when the interface presents many irregular features. As an example, the superposition of the as-detected

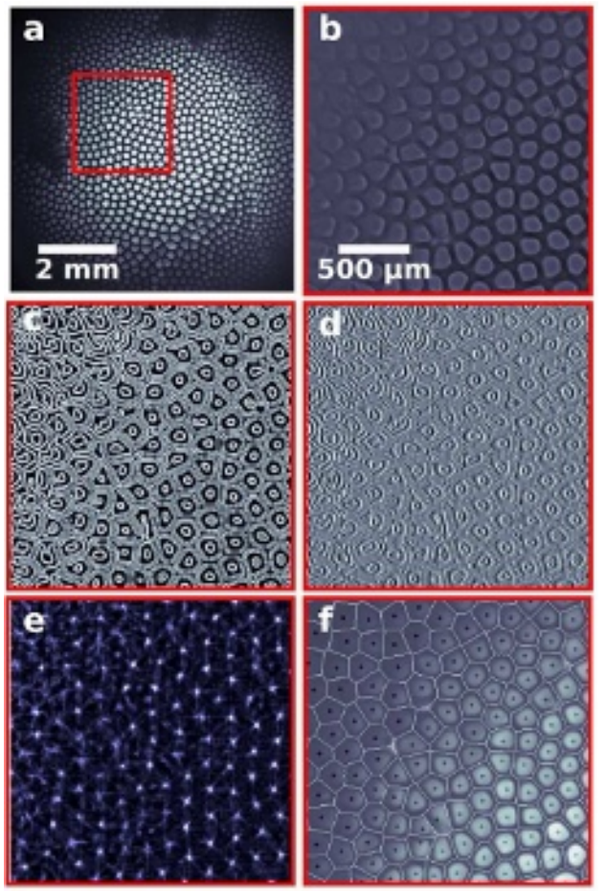

FIG. 6. Intermediary steps produced by the concentric feature algorithm: (a) raw image; (b) zoomed region of the normalized image; (c) edge-enhanced image; (d) Sobel filtered edges; (e) ledger of concentric features; (f) centers and segmentation of image. The zoom was applied to the red square of (a).

centers to the raw image is given in Figure 7b. The computation is not perfect due to the lack of homogeneity within the image contrast, therefore this method can be coupled, for better results, to the post treatment methods described in Section III F.

D. Dendrite centers identification by FFT

The main difficulty encountered in identifying dendrite centers is to distinguish between the main trunk tip and the secondary branches that can exhibit similar brightness. Even after a local equalization rank filter[28] (Figure 8a), the vast majority of images have features that cannot be binarized by a single threshold value. In order to remove the information on the secondary branches so that the algorithm can focus on the very centers, the Fast Fourier Transform (FFT) is applied on the dispersion image. The dispersion image represents, for each pixel, the standard deviation of the pixel values contained in a patch of a given size and centered on the pixel of interest

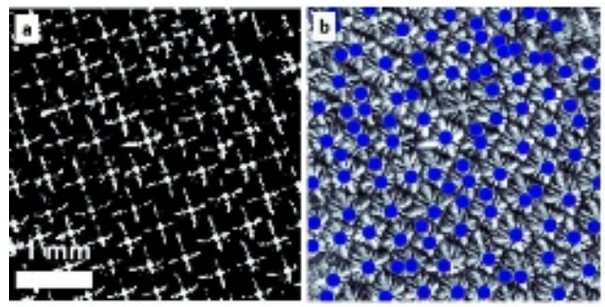

FIG. 7. Intermediary steps produced by the threshold centers identification method: (a) binary image applying a threshold below which the groove is considered; (b) centers superimposed to the raw image.

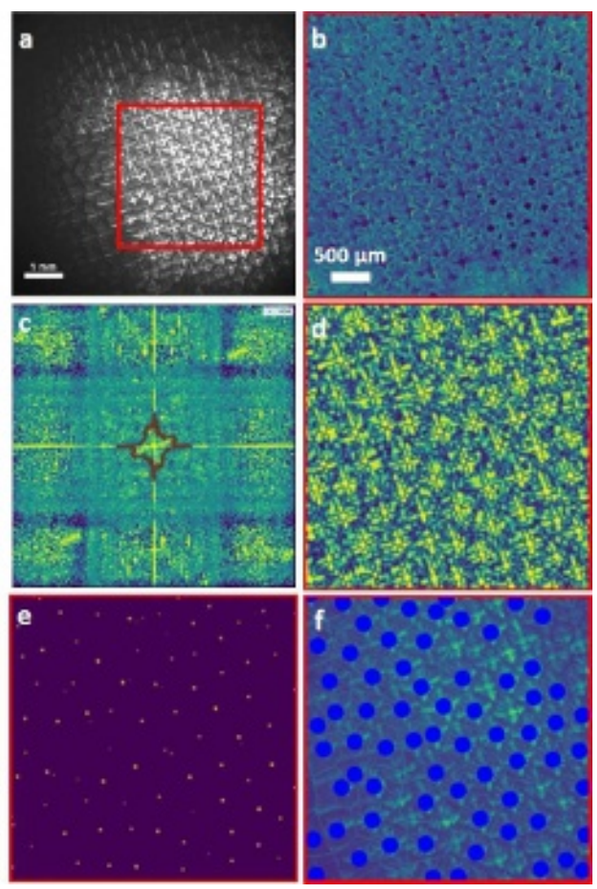

FIG. 8. Intermediary steps produced by the FFT centers identification method: (a) raw image ; (b) dispersion image; (c) FFT of the dispersion image; (d) Inverse Fourier Transform of the image with just the low frequencies inside the brown contour of c; (e) binary image representing the tip of the dendrites from applying a threshold on (d); (f) centers and segmentation superimposed to the raw image. The red squared region in a is represented in b, d, e and f.

(Figure 8b).

A low-pass filter is then applied to the dispersion image, considering a fixed threshold (in the range of 0 to 1). The goal is to choose a threshold value such that the contour reproduces the canonical shape of the dendrites, which should appear on the FFT (the cross in Figure 8c). Figure 8d shows the inverse Fourier Transform of the image with just the low frequencies inside the brown contour of Figure 8c. Finally, the position of the dendrites can be computed by threshold this inverse FFT image (Figure 8e). The value of this threshold is chosen very close to unity to specifically image only tip centers.

The outcome gives satisfying results (Figure 8f). The computation, however, is once again not perfect due to the lack of homogeneity within the image contrast and this method can be coupled, for better results, to the post treatment methods (Section III F).

E. Characteristic size by FFT

Some images cannot be treated by the previous methods, especially those obtained during the transient step of microstructure formation, for example as shown in Figure 9a, because amplitudes are too small and resulting contrasts very low. Despite this limitation, it is possible to quantify the evolution of the characteristic size of this early interface pattern by analyzing the Fourier spectrograms of the image.

A Fourier transform of a bitmap image in spatial domain maps its characteristics to the frequency domain. Each spatial vector in the Fourier transformed image corresponds to a wave vector of the original image. The Discrete Fourier Transform (DFT) is used, implemented by the Fast Fourier Transform function in the NumPy library[28] of the Python scripting language.

This procedure computes the FFT image of the whole interface, or a squared portion of it, and plots the radially averaged power spectrum (RAPS) and its derivative. The RAPS is the direction-independent mean spectrum, i.e. the average of all possible directional power spectra. It provides a convenient means to view and compare the information contained in 2D spectra in 1D. The frequency axis of the main peak is associated with the primary spacing.

This technique was applied for each one of the squared portions in Figure 9a, and the respective RAPS and its derivatives were obtained, as exemplified in Figure 9b in blue (single lines) for the zoomed region in Figure 9a. The peaks in the 1D power spectrum correspond to the characteristic sizes of the microstructure. In this example, the interface shows a corrugation of spacing approximately 99 m. Applying the same procedure in each squared patch, the average primary spacing is equal to 90.6 ± 9.8 m at this early moment.

To validate this technique, an image with an established dendritic pattern was used to perform a comparison (it was applied to the red squared region in Figure 8a). The characteristic distance estimated from the FFT image and the corresponding RAPS is 395 m (double lines in red in Figure 9b). When identifying the centers by the threshold method in the same region, the histogram of the primary spacings leads to an average value of 409 ± 56 m (Figure 9c). The distributions obtained from the two different methods are in very good agreement, with less than 5% difference, thus validating the use of the FFT method.

F. Post-treatment and local image treatment

The input to the methods described above is a greyscale image, and the output is a set of coordinates of the centers of cells/dendrites. As previously mentioned, producing an efficient center finder algorithm is difficult. For example, for dendrites, a way to successfully recover the centers is to first slightly overestimate the center detection (Figure 10a). Then, each individual dendrite's shape is extracted using a threshold definition over the whole interface (as exemplified in Figure 10b for the dendrite surrounded by the green line in a). The eigenvectors, drawn in red and blue in Figure 10b, enable computation of the orientation of the dendrites. The angle of the principal eigenvector (defined by the red line with respect to the horizontal) is 15 for this particular dendrite. From all the centers pointing to the same extracted shape, only the one closest to the shape centroid is kept. Finally, the redundant centers are removed (Figure 10c). This time-consuming procedure is combined with the previously defined center identification procedures.

It is also possible to manually interfere in the output containing the centers to delete a center that was erroneously counted or add a center that was not counted. The corrections are done through the raw image with the centers superimposed.

The procedure of finding the cells/dendrites centers is repeated for each successive image of the interface, to obtain a large set of coordinates (x, y) and t. Then, a powerful clustering algorithm, the Density-Based Spatial Clustering of Applications with Noise (DBSCAN)[29,30], is used to link the label of each cell or dendrite through time. It will consider all the centers, from all the images, as a 3D scatter plot, and it will try to isolate individual clusters corresponding to the time evolution of each cell or dendrite coordinates. In order to isolate the individual clusters, three main user-defined parameters are adjusted: ε, the radius of the sphere used by DBSCAN to decide if two cells/dendrites belong to the same cluster; *time_compressor*, the virtual spacing between two images, setting an axis in the temporal direction (consistent with the spacing between cells belonging to the same image); and *min_sample*, the minimum number of cores necessary to consider a group of cells as a cluster. The $(x(t), y(t))$ succession of coordinates is used to calculate cell/dendrite top-view apparent velocity (defined as drift velocity). The clusters computation also helps to correct erroneous identification during the computation of centers. Figure 11a shows an example where the centers detected by the FFT or thresholding methods (in blue) are compared to the ones resulting from the clusters computation (in yellow). Using the basic methods, the dendrites surrounded by dashed green lines had two centers detected, and those surrounded by full cyan lines were not detected. After, the clusters computation, they are correctly

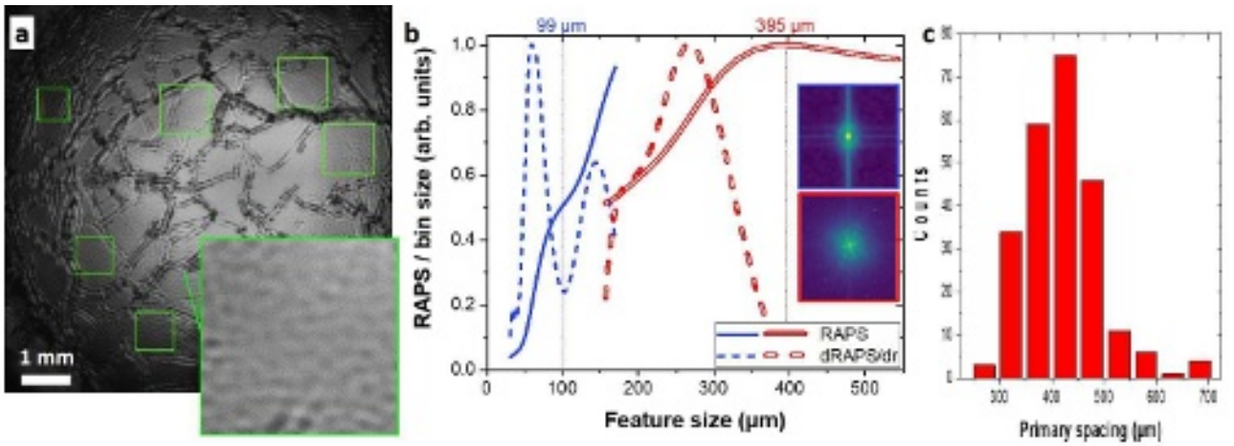

FIG. 9. (a) Top view and detail of the solidification interface during the early stages of morphological instability development (Exp2: SCN–0.46 wt% camphor, V = 3 m/s, G = 12 K/cm, L = 2.3 mm). (b) Radially averaged power spectrum (RAPS) and its derivative, and corresponding FFT images, for the detail of (a) in blue (single lines), and the red squared region of Figure 8a in red (double lines). (b) Histogram of the primary spacing after centers detection by thresholding method (Section III C) for the red squared region of Figure 8a.

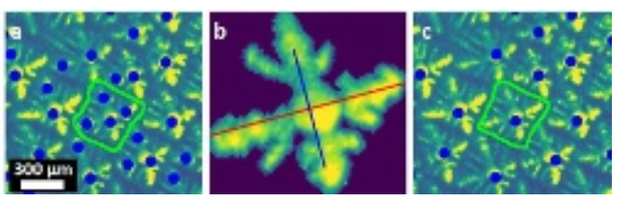

FIG. 10. Dendrite centers superimposed to the raw image: (a) overestimated and (c) after the application of the cleaning procedure. (b) Extracted shape of the dendrite surrounded by a green line where the eigenvectors are drawn in red and blue.

considered.

After the segmentation and time-labeling of each experiment, the information necessary to extract the physical characteristics with interest and to follow their evolution in time are available. The methods allow identification of each center, and a Voronoi tessellation of the centers reliably finds their first neighbors (see example in Figure 11b). A database of first neighbors, the primary spacing of each cell or dendrite, and its position at all times during the experiment are obtained. The maps of number of neighbors, position in time, velocity, and primary spacing can then be calculated. Furthermore, precise statistics and their evolution on the entire interface or by region can be calculated.

The cell or dendrite shape characteristics, in particular tip radius, local growth rate, secondary branching, can be obtained by reconstruction of the interferometric fringes. The associated methods are given in details in a previous publication[19].

IV. RESULTS

To illustrate the use of the methods described above, two experiments performed onboard ISS were analyzed: one performed during the first flight campaign with a sample of SCN-0.24 wt% camphor at V = 4 m/s and G = 19 K/cm (here named Exp1, supplementary video S1); and another during the second flight campaign with a sample of SCN-0.46 wt% camphor at V = 3 m/s and G = 12 K/cm (here named Exp2, supplementary video S2). As mentioned before, the experimental campaigns were started with a single crystal, with a <100> direction aligned with the pulling axis as closely as possible (Figure 4). Due to the several melting-solidification cycles, a progressive increase of sub-boundaries was noticed that was attributed to thermomechanical stresses that lead to re-organizations of dislocations. A sub-grain (SG) is characterized by its crystallographic orientation, that is its specific tilt compared to the pulling direction; a sub-boundary (SB) defines the limit between two different SGs. SB is an unavoidable and extremely frequent defect of the solid seed, so that numerous SBs are observed that may influence microstructure evolution. The microstructure formation is quite similar regardless of the type of experiments[14,31]. After motion being triggered, the morphological instability first initiates along sub-boundaries before developing as a uniform corrugation. The amplitude of all interface modulations increases and grooves start to form, but it is still difficult to identify the microstructures. At this stage, the interface dynamics is remarkably fast and the pattern disorder high. In this work, disorder is mainly evidenced by characterizing defects of the pattern. In an hexagonal pattern, each structure whose first neighbors do not number 6 is seen as a defect. There is then a progressive decrease in disorder, and a clear pattern eventually emerges. The dynamics then slows down and is limited to progressive size adjustments and array ordering. Exp1 eventually led to a cellular pattern, whereas Exp2 to a dendritic

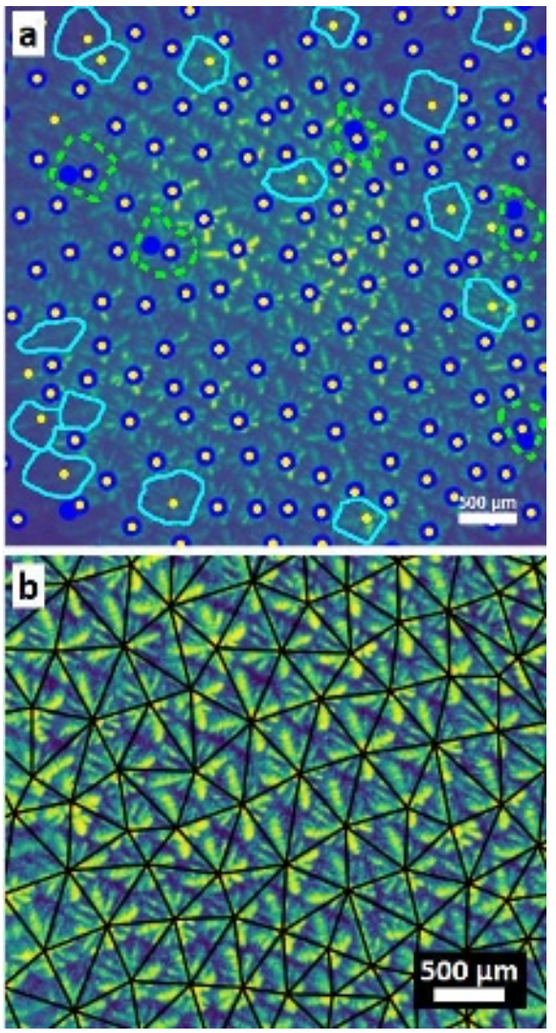

FIG. 11. (a) Comparison between the centers detected by the classical methods (in blue) and the clusters computation (in yellow) leading to several improvements: the dendrites surrounded by dashed green lines were overestimated by the classical methods and by full cyan lines not detected. (b) Zoom on the central region with the Voronoi tessellation from the centers of dendrites.

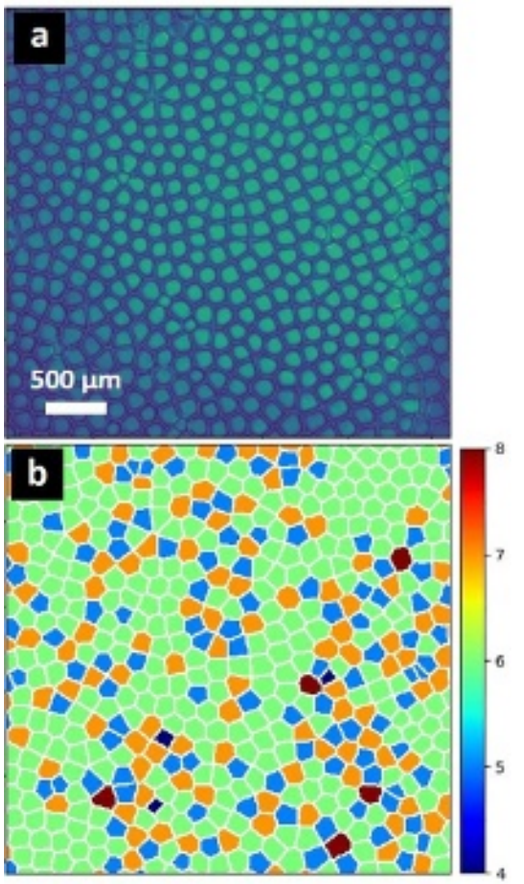

FIG. 12. (a) Detail of the interface after 4 h of pulling (or 59.5 mm) for Exp1 (SCN–0.24 wt% camphor, V = 4 m/s, G = 19 K/cm). (b) Corresponding number of first neighbors map.

pattern.

The number of nearest neighbors was determined using the Voronoi tessellation, which gives information on the quantity of topological defects in the pattern. A perfect hexagonal tiling would correspond to six nearest neighbors for each cell/dendrite. On both experiments, there is a high number of topological defects that are mainly instances of five and seven nearest neighbors (for instance Figure 12 for Exp1). Such penta-hepta defects are commonly observed both experimentally[16,32] and computationally[33] in disordered hexagonal cellular array patterns formed during directional solidification. More broadly, they are characteristic defects of hexagonal patterns formed in a wide variety of non-equilibrium systems in fluid dynamics, optics, and chemical kinetics[34–36].

The possibility of in situ visualization of the solidification allows the characterization of the patterns as a function of time (or solidified length $L = V.t$). The primary spacing λ, one of the most fundamental characteristics, was for example followed during the whole solidification. The primary spacing of each cell or dendrite was calculated and the evolution of its average value studied (Figure 13). On Exp1, from $L = 5$ mm the cellular pattern was sufficiently developed to apply the image treatment procedures previously presented (Sections III A and III B). The primary spacing presents a slight overshoot, with a maximum of 222 m, before decreasing to reach a stable spacing around 192 m at 22 mm. On Exp2, the data points after $L = 4$ mm, $\lambda = 384$ m, were obtained applying the procedures of dendrite centers identification presented in Sections III C and III D, as the dendritic pattern was sufficiently developed. It was not possible to determine the spacing in the early stages of microstructure formation with center-to-center methods because the grooves between cells or primary dendrites were not deep enough. Therefore, the initial estimation of the average λ was performed using the fast Fourier transform (FFT) analysis (Section III E), as exemplified for the very first moments in Figure 9a and b (2.3 mm of solidification). The FFT analy-

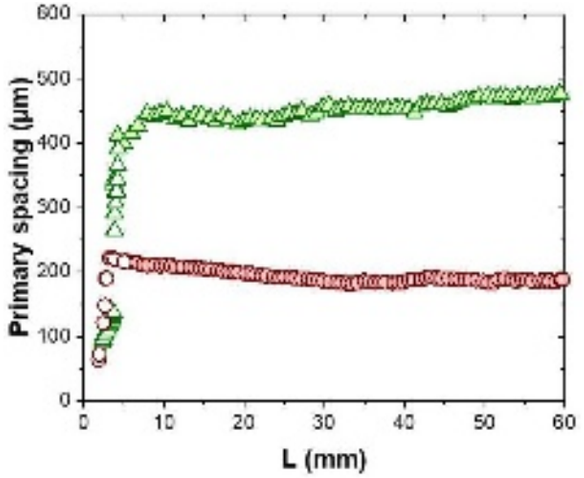

FIG. 13. Primary spacing evolution as a function of the solidified length L: red circles for Exp1 (SCN–0.24 wt% camphor, V = 4 m/s, G = 19 K/cm), and green triangles for Exp2 (SCN–0.46 wt% camphor, V = 3 m/s, G = 12 K/cm). In order to simplify visualization, only 1 out of 10 points are shown for Exp1 and 1 out of 3 for Exp2, and the standard deviations are not represented (in average 30 m for Exp1 and 48 m for Exp2). The open symbols were determined using the techniques described in Section III E.

sis only pertains to the early stage, i.e. at most the first 5 mm of solidification in Figure 13 (empty symbols), and is found to provide a good continuity and overlap with the more accurate center-to-center analysis where both methods are applicable.

In both experiments, the image sequence revealed cells and dendrites that drift along the interface (see supplementary videos S1 and S2). This drift in quite apparent in top-view images, and originates in a tilt of the growth direction compared to the pulling direction, meaning that a growth velocity component exists in the plane of the image[37,38]. The only obvious way to identify SGs, and therefore SB, is to analyze the pattern drift velocity that directly results from tilt characteristics. Each SG is characterized by a collective drift of dendrites, of specific direction and amplitude, caused by its particular misalignment to the pulling/thermal axis.

The microstructure in Exp2 was not strikingly different within the interface, but it was noticed that there were areas characterized by different drifting directions, following this observation the different SGs were identified by grouping dendrites with similar drifting directions. Figure 14a and b show each dendrite velocity magnitude and direction, respectively, after around 50 mm of solidification. Due to small misorientations, both directions and amplitudes were required to discriminate the SGs, and several successive images were used to validate the location of SBs, which were freehand drawn in Figure 14. Sub-grains were then named as indicated. The dendrites of SGs 1 and 2 move in slightly different directions: approximately -45 for SG2 and -55 for SG1 (measured counterclockwise with right = 0).

The time evolution of the primary spacing maps extracted from the image sequence for Exp2 revealed that initially the

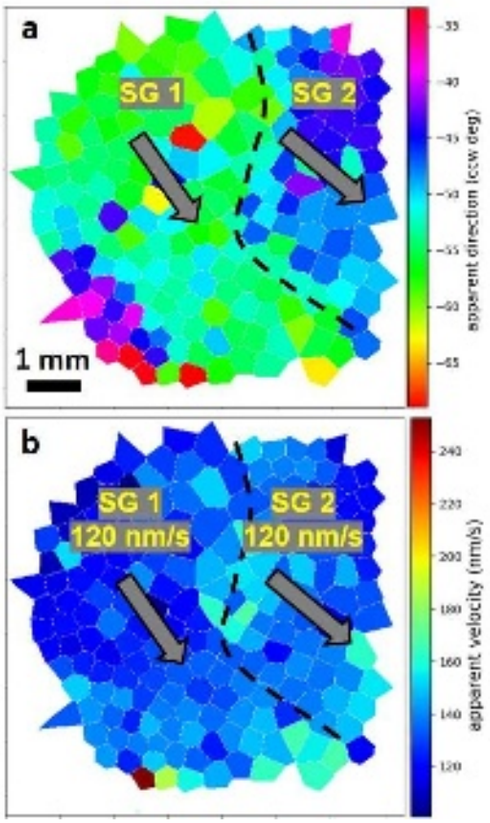

FIG. 14. (a) Drifting direction and (b) velocity amplitude maps at 50 mm of solidification, where two sub-grains (SG) are distinguished and the dashed line corresponds to the sub-boundary. The arrows indicate the average drifting direction, and the values in (b) indicate the average drifting velocity amplitude. (Exp2: SCN-0.46 wt% camphor, V = 3 m/s, G = 12 K/cm)

spacing was highly dispersed all along the interface (Figure 15a). As growth progresses, dispersion progressively decreased and there was no clear evidence of ordered variation of spacing, except a line of large spacings at the top center (clearly distinguished at 59 mm). The origin of this local high spacing is the existence of a divergent sub-boundary, similar to what was found in the cellular regime[14]. It led to a local stretching of microstructures, and consequently this line of local high spacing, and also the development of secondary branches (Figure 15b).

V. CONCLUSIONS

In this paper, the experimental framework of the Directional Solidification Insert of the DECLIC device installed on board ISS is detailed. The flight experiments consist of directional solidification of succinonitrile-based alloys in a cylindrical ampoule, and provide a unique opportunity to observe the formation and evolution of directionally solidified 3D extended arrays of cells and dendrites in diffusive transport conditions.

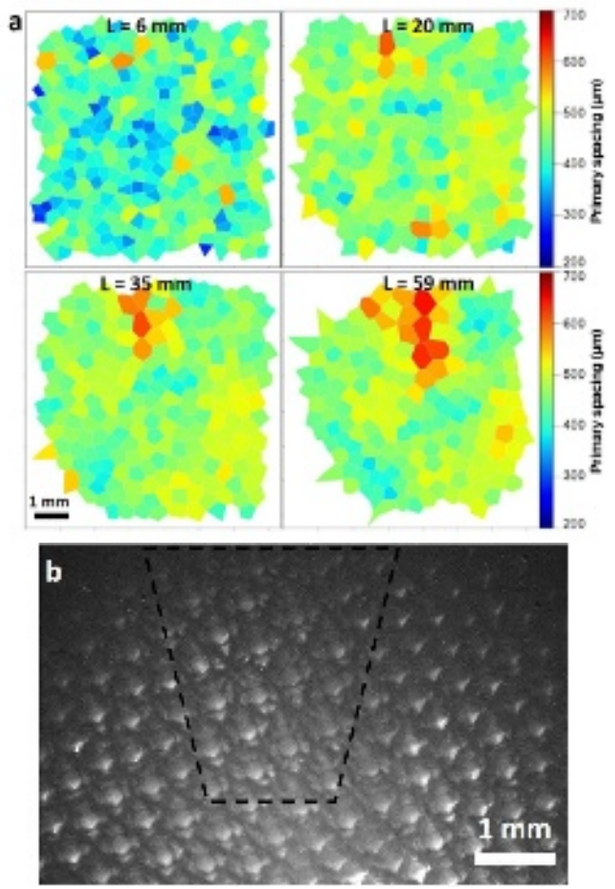

FIG. 15. (a) Primary spacing maps for solidified lengths L from 6 to 59 mm. (b) Zoom at the border of the crucible evidencing the development of secondary branches. (Exp2: SCN-0.46 wt% camphor, V = 3 m/s, G = 12 K/cm)

By systematically varying the process parameters (concentration, pulling rate, thermal gradient), the experiments are critically important to establish benchmark comparisons with computational modeling predictions. The procedures developed over the last few years to robustly analyze extremely large image datasets obtained by direct axial observation are described. These procedures allow to quantitatively study the complex microstructure dynamics that occur at the solidification interface in terms of spacing, number of first neighbors and gliding velocity/direction. This is illustrated with two experiments where cellular and dendritic patterns were obtained.

Understanding the dynamics of pattern formation is a promising challenge, and the microgravity environment allows observation of fundamental phenomena that arise during large-scale bulk solidification. To this end, the quantitative and powerful methods of data treatment that were developed are invaluable tools. In addition to providing insight into the dynamics of interface pattern formation, the dendritic microstructural patterns that evolve have direct technological relevance for the solidification and casting industry.

SUPPLEMENTARY MATERIAL

See the supplementary material for the experimental videos showing in situ observations during microgravity directional solidification of succinonitrile-camphor alloys, using two sets of experimental parameters. The optical images were recorded from a camera with an immersed lens in the liquid directly facing the solidification front main growth direction.

ACKNOWLEDGMENTS

The authors gratefully acknowledge J. Pereda and S. Quiret who highly contributed to the development of the automated treatment. This project is supported by the French Space Agency CNES (Microstructures de solidification 3D - MISOL3D – project) and NASA (grant 80NSSC22K0664 - Spatiotemporal Evolution of Three-Dimensional Dendritic Array Structures - SPADES – project).

CONFLICT OF INTEREST

All authors declare that they have no conflicts of interest.

DATA AVAILABILITY STATEMENT

The data that support the findings of this study are available from the corresponding author upon reasonable request.

REFERENCES

[1]M. C. Cross and P. C. Hohenberg, Reviews of Modern Physics **65**, 851 (1993).
[2]B. Billia and R. Trivedi, "Pattern formation in crystal growth," in *Handbook of Crystal Growth*, Vol. 1, edited by D. Hurle (North-Holland, Bristol, 1993) Book section Part B. 14, pp. 899–1074, 1st ed.
[3]K. A. Jackson and J. D. Hunt, Acta Metallurgica **13**, 1212 (1965).
[4]H. Jamgotchian, N. Bergeon, D. Benielli, P. Voge, B. Billia, and R. Guerin, Physical Review Letters **87**, 6105 (2001).
[5]N. Bergeon, G. Reinhart, F. L. Mota, N. Mangelinck-Noel, and H. Nguyen-Thi, The European physical journal. E, Soft matter **44**, 98 (2021).
[6]F. L. Mota, Y. Song, J. Pereda, B. Billia, D. Tourret, J. M. Debierre, R. Trivedi, A. Karma, and N. Bergeon, JOM **69**, 1280 (2017).
[7]L. Sturz, G. Zimmermann, M. Mathes, S. Rex, and B. Kauerauf, Metallurgical and Materials Transactions a-Physical Metallurgy and Materials Science **35A**, 239 (2004).
[8]B. Kauerauf, G. Zimmermann, S. Rex, B. Billia, H. Jamgotchian, and J. D. Hunt, Journal of Crystal Growth **223**, 277 (2001).
[9]B. Kauerauf, G. Zimmermann, S. Rex, M. Mathes, and F. Grote, Journal of Crystal Growth **223**, 265 (2001).
[10]N. Bergeon, F. L. Mota, J. Pereda, D. Tourret, Y. Song, J. M. Debierre, R. Guerin, A. Karma, R. Trivedi, and B. Billia, International Journal of Microgravity Science and Application **33**, 6 (2016).
[11]F. L. Mota, N. Bergeon, D. Tourret, A. Karma, R. Trivedi, and B. Billia, Acta Materialia **85**, 362 (2015).
[12]Y. Song, D. Tourret, F. L. Mota, J. Pereda, B. Billia, N. Bergeon, R. Trivedi, and A. Karma, Acta Mater **150**, 139 (2018).
[13]F. L. Mota, K. Ji, L. S. Littles, R. Trivedi, A. Karma, and N. Bergeon, Acta Materialia , 118849 (2023).

[14]F. L. Mota, J. Pereda, K. Ji, Y. Song, R. Trivedi, A. Karma, and N. Bergeon, Acta Materialia **204**, 116500 (2021).
[15]Y. Song, F. L. Mota, D. Tourret, K. Ji, B. Billia, R. Trivedi, N. Bergeon, and A. Karma, Nature Communications **14**, 2244 (2023).
[16]J. Pereda, F. L. Mota, L. Chen, B. Billia, D. Tourret, Y. Song, J. M. Debierre, R. Guérin, A. Karma, R. Trivedi, and N. Bergeon, Physical Review E **95**, 2803 (2017).
[17]N. Bergeon, D. Tourret, L. Chen, J. M. Debierre, R. Guerin, A. Ramirez, B. Billia, A. Karma, and R. Trivedi, Physical Review Letters **110**, 6102 (2013).
[18]D. Tourret, J.-M. Debierre, Y. Song, F. Mota, N. Bergeon, R. Guérin, R. Trivedi, B. Billia, and A. Karma, Physical Review E **92**, 2401 (2015).
[19]J. Pereda, F. L. Mota, J. M. Debierre, B. Billia, R. Trivedi, A. Karma, and N. Bergeon, Physical Review E **102**, 032804 (2020).
[20]F. L. Mota, N. Bergeon, A. Karma, R. Trivedi, and J. M. Debierre, Physical Review E **102**, 12 (2020).
[21]N. Noel, F. Zamkotsian, H. Jamgotchian, and B. Billia, Measurement Science and Technology **11**, 66 (2000).
[22]N. Bergeon, C. Weiss, N. Mangelinck-Noel, and B. Billia, Transactions of the Indian Institute of Metals **62**, 455 (2009).
[23]H. Jamgotchian, N. Bergeon, D. Benielli, P. Voge, and B. Billia, Journal of Microscopy-Oxford **203**, 119 (2001).
[24]S. Liu, P. Mazumder, and R. Trivedi, Journal of Crystal Growth **240**, 560 (2002).
[25]M. Kurz, A. Pusztai, and G. Muller, Journal of Crystal Growth **198**, 101 (1999).
[26]M. Kurz, *Development of CrysVUN++, a software system for numerical modelling and control of industrial crystal growth processes.*, Thesis (1998).
[27]N. Bergeon, A. Ramirez, L. Chen, B. Billia, J. Gu, and R. Trivedi, Journal of Materials Science **46**, 6191 (2011).
[28]S. van der Walt, S. C. Colbert, and G. Varoquaux, Computing in Science and Engineering **13**, 22 (2011).
[29]F. Pedregosa, G. Varoquaux, A. Gramfort, V. Michel, B. Thirion, O. Grisel, M. Blondel, P. Prettenhofer, R. Weiss, V. Dubourg, J. Vanderplas, A. Passos, D. Cournapeau, M. Brucher, M. Perrot, and E. Duchesnay, Journal of Machine Learning Research **12**, 2825 (2011).
[30]R. J. G. B. Campello, D. Moulavi, and J. Sander (Springer Berlin Heidelberg) pp. 160–172.
[31]N. Bergeon, F. L. Mota, L. Chen, D. Tourret, J. M. Debierre, R. Guerin, A. Karma, B. Billia, and R. Trivedi, IOP Conference Series-Materials Science and Engineering **84**, 012077 (2015).
[32]B. Billia, H. Jamgotchian, and H. Nguyen-Thi, Metallurgical Transactions a-Physical Metallurgy and Materials Science **22**, 3041 (1991).
[33]T. Takaki, S. Sakane, M. Ohno, Y. Shibuta, T. Shimokawabe, and T. Aoki, Acta Materialia **118**, 230 (2016).
[34]E. Bodenschatz, J. R. Debruyn, G. Ahlers, and D. S. Cannell, Physical Review Letters **67**, 3078 (1991).
[35]W. J. Firth, Chaos in Optics **2039**, 290 (1993).
[36]Q. Ouyang and H. L. Swinney, Nature **352**, 610 (1991).
[37]C. Weiss, N. Bergeon, N. Mangelinck-Noel, and B. Billia, Physical Review E **79**, 1605 (2009).
[38]S. Bottin-Rousseau and A. Pocheau, Physical Review Letters **87**, 6101 (2001).

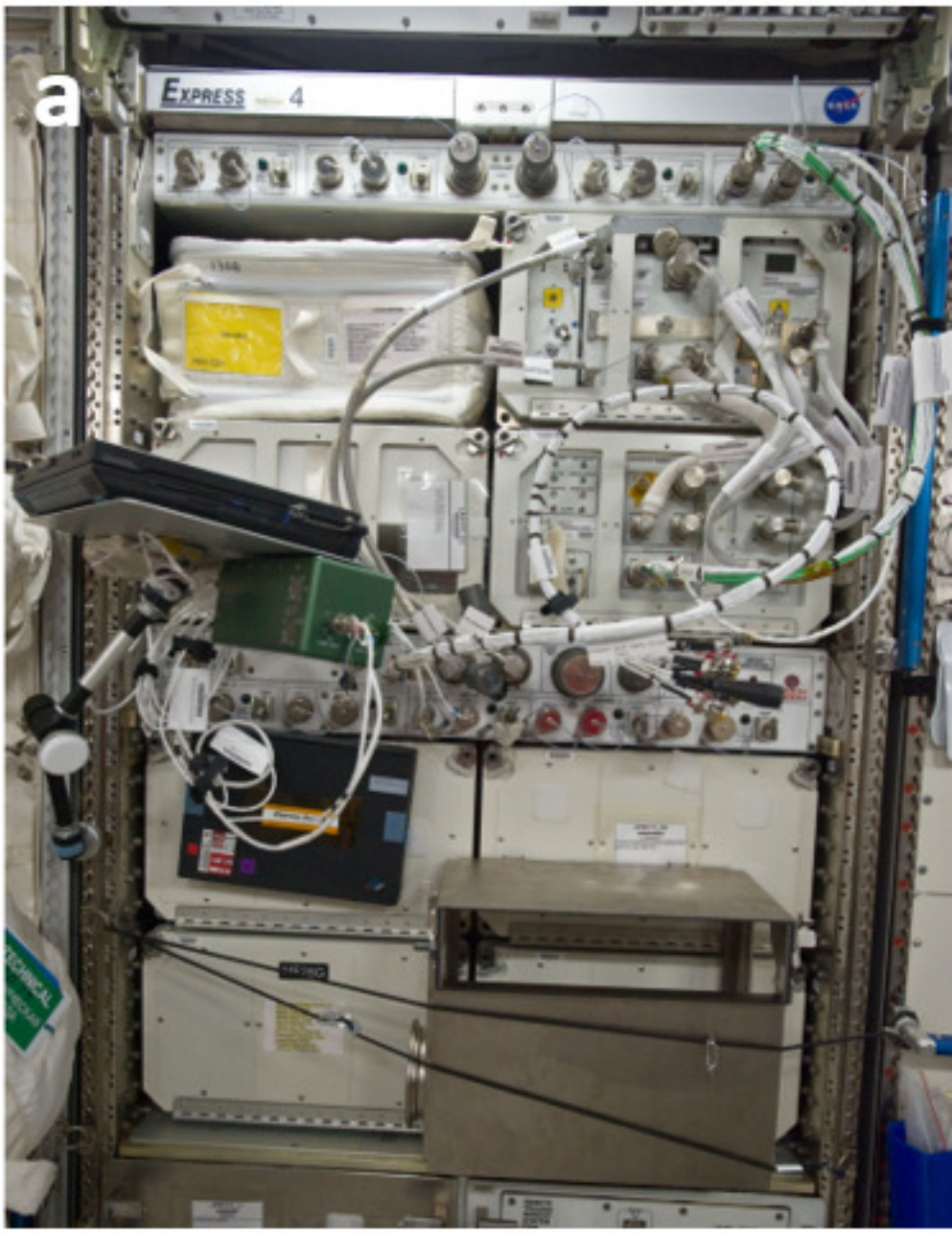
a
EXPRESS 4

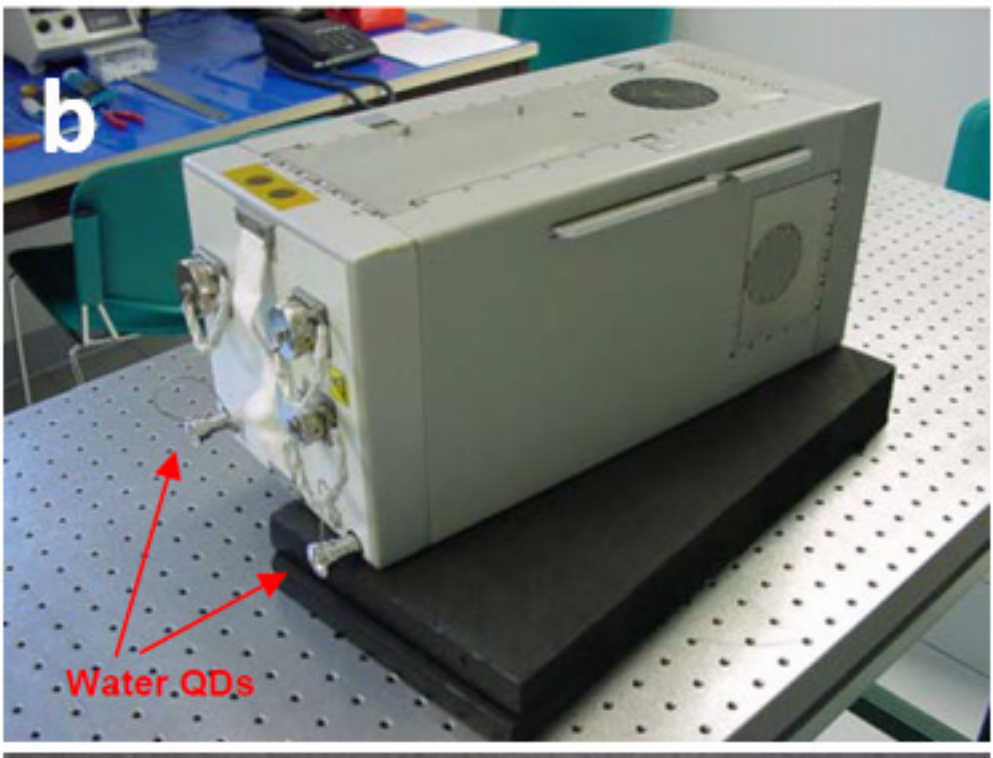
b
Water QDs

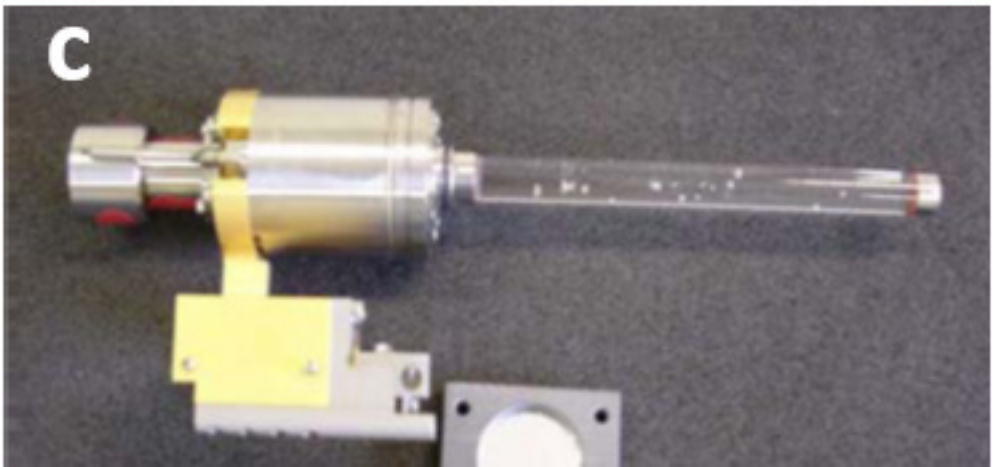
c

a

b

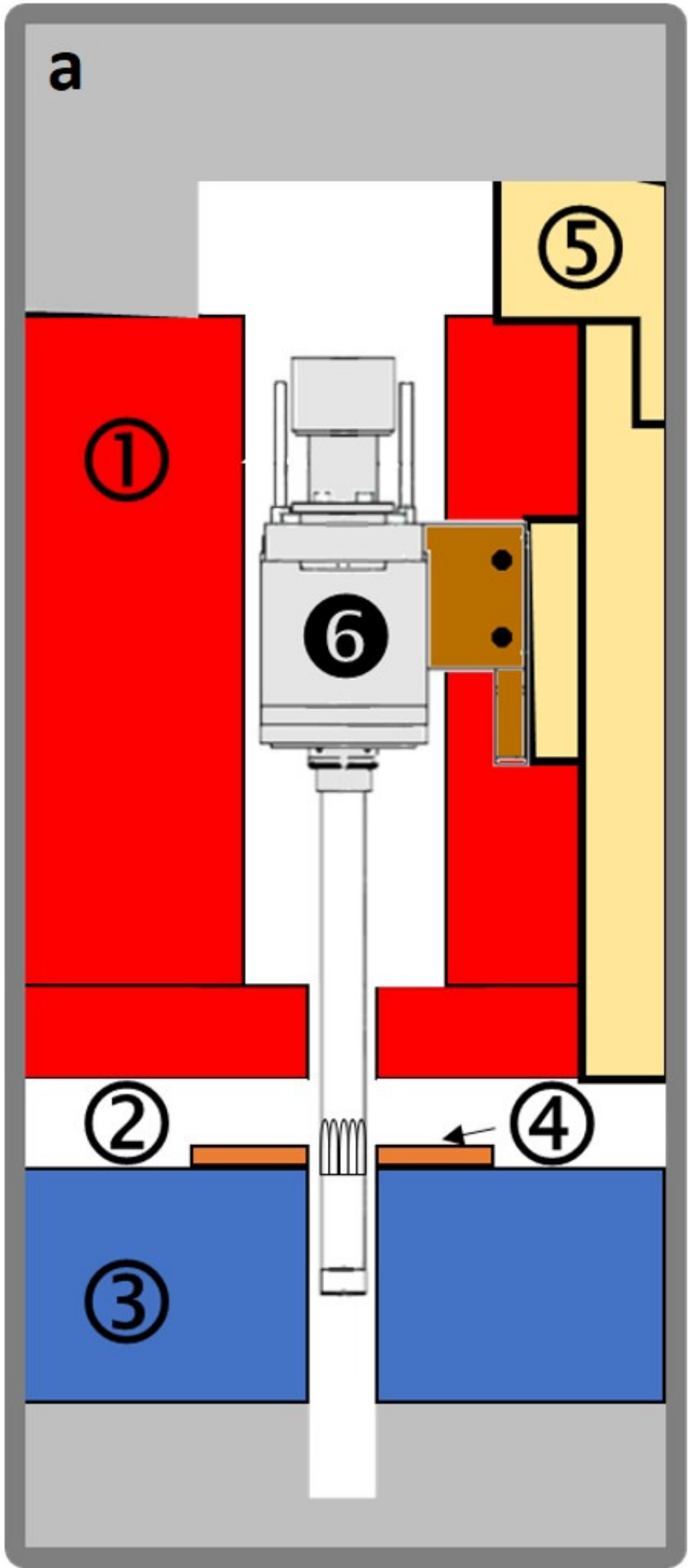

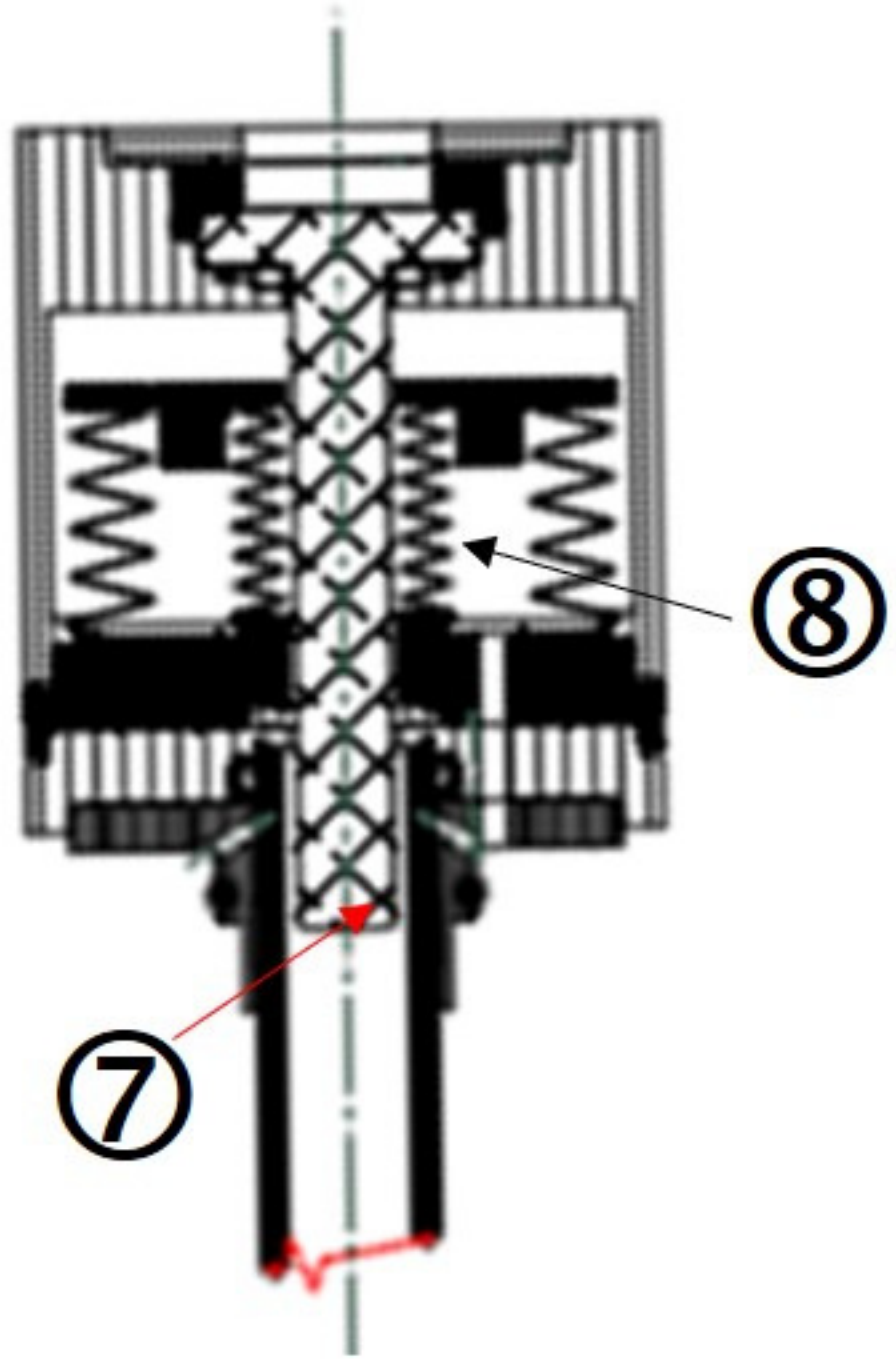

a

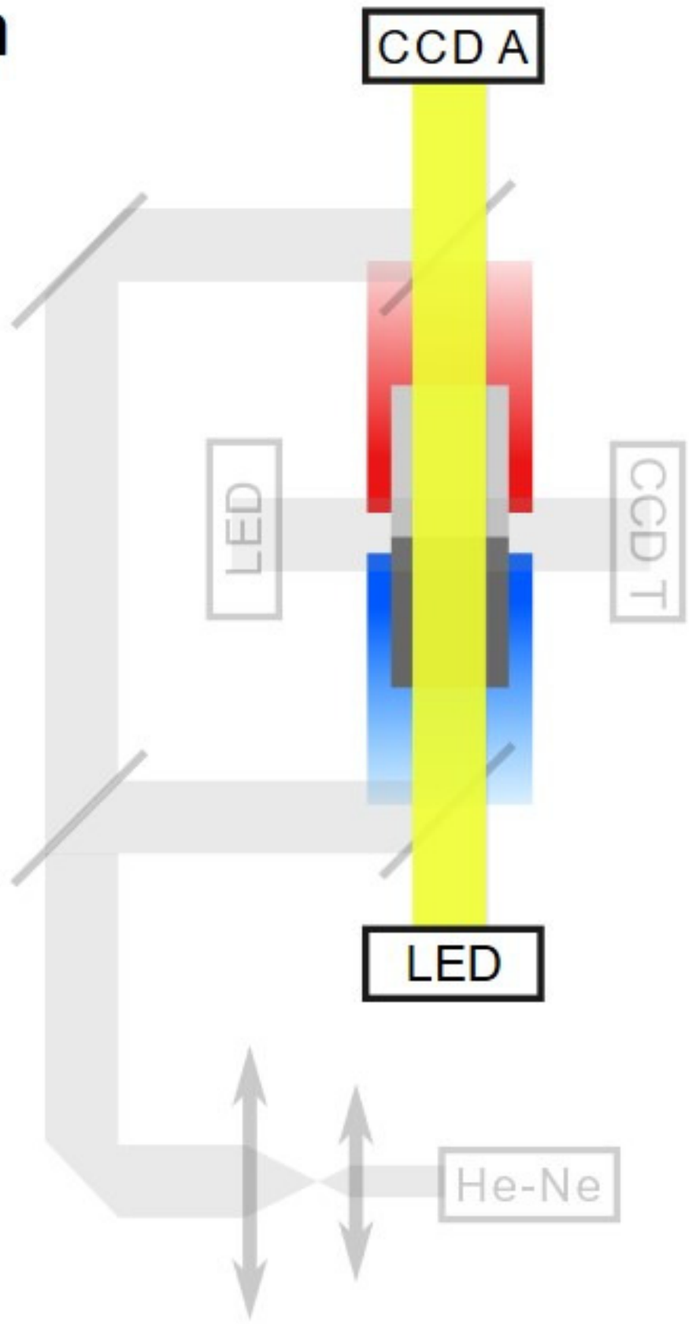
CCD A
LED
CCD T
LED
He-Ne

b

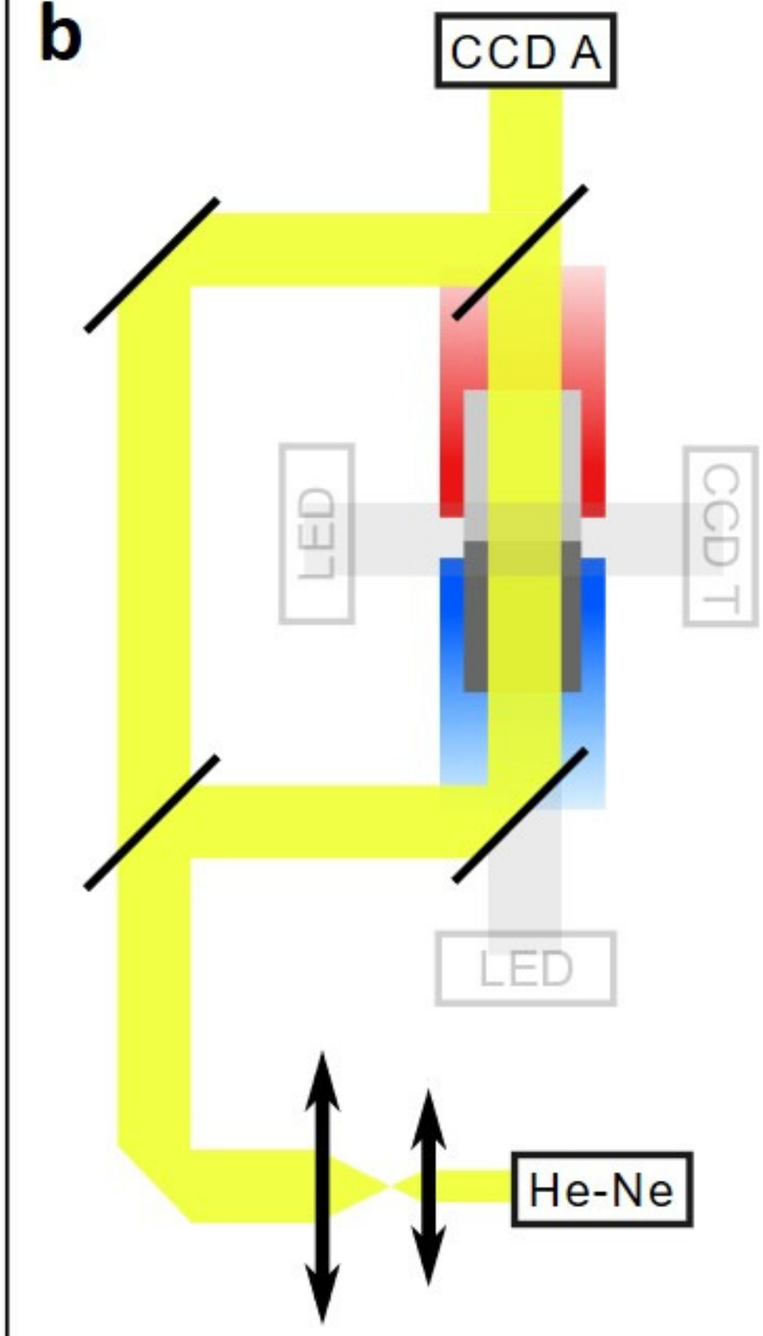
CCD A
LED
CCD T
LED
He-Ne

c

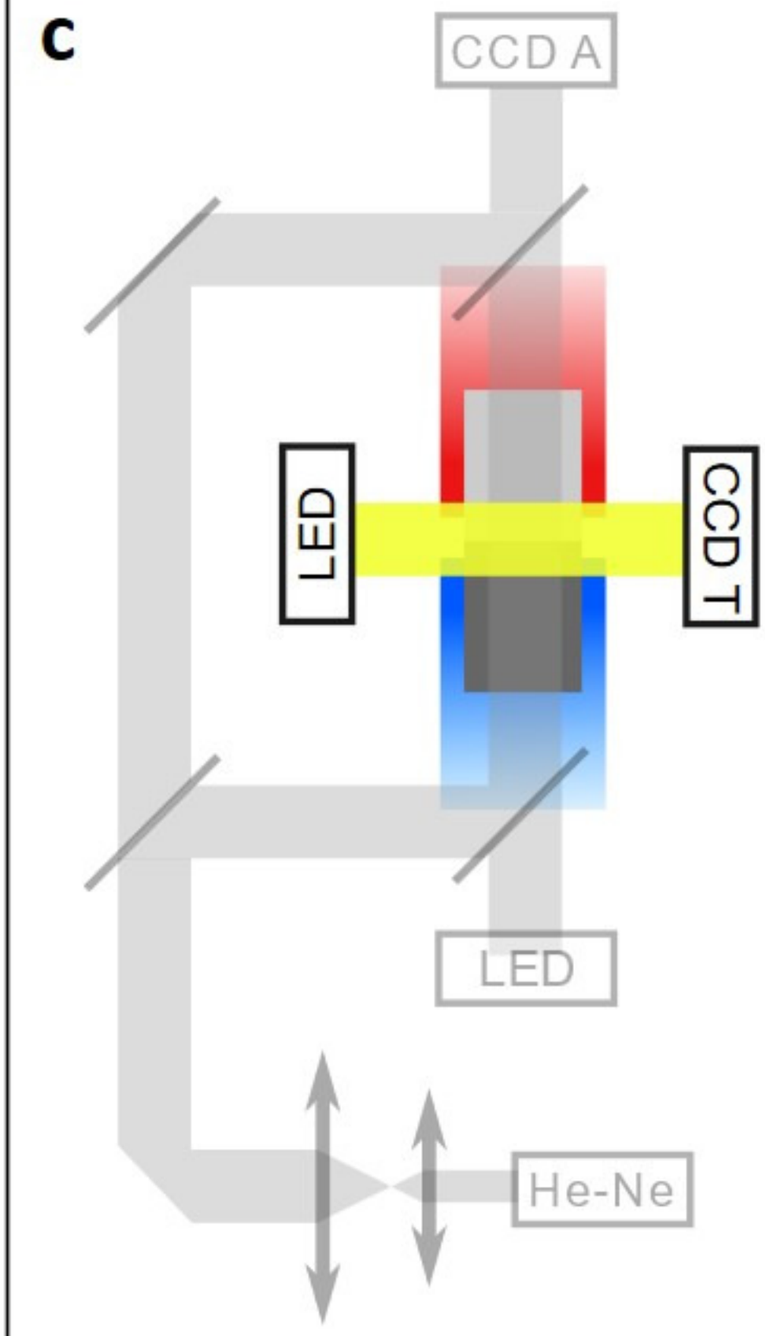
CCD A
LED
CCD T
LED
He-Ne

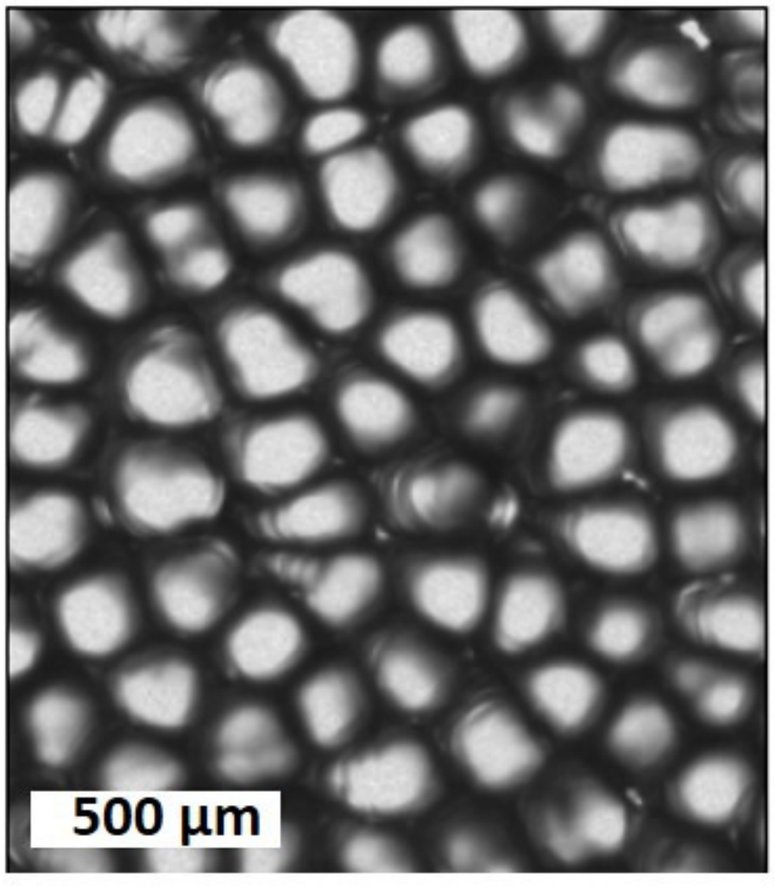
500 µm

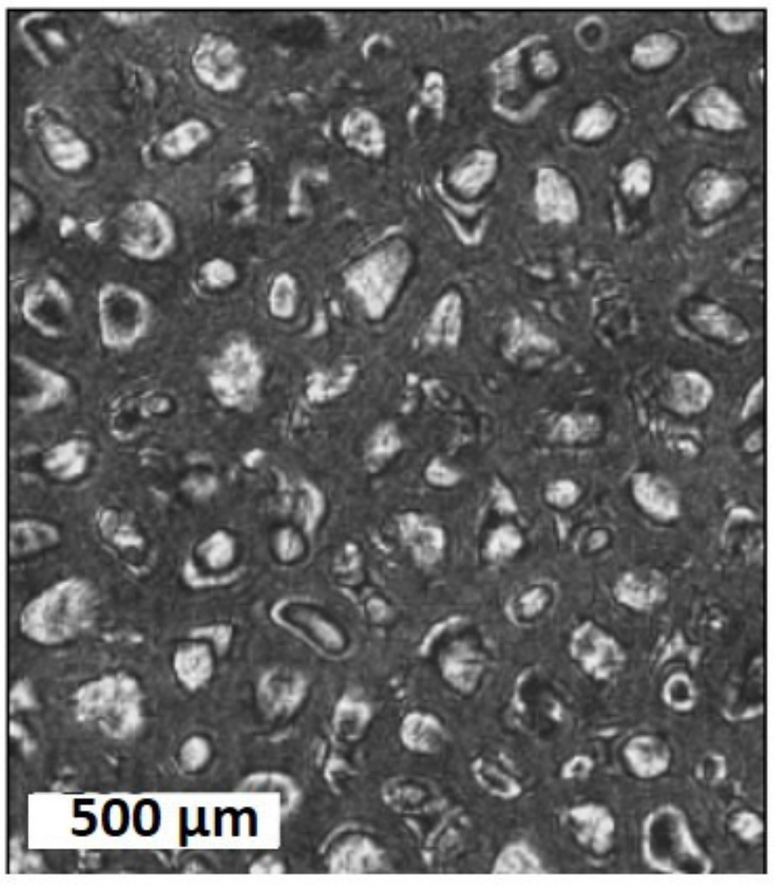
500 µm

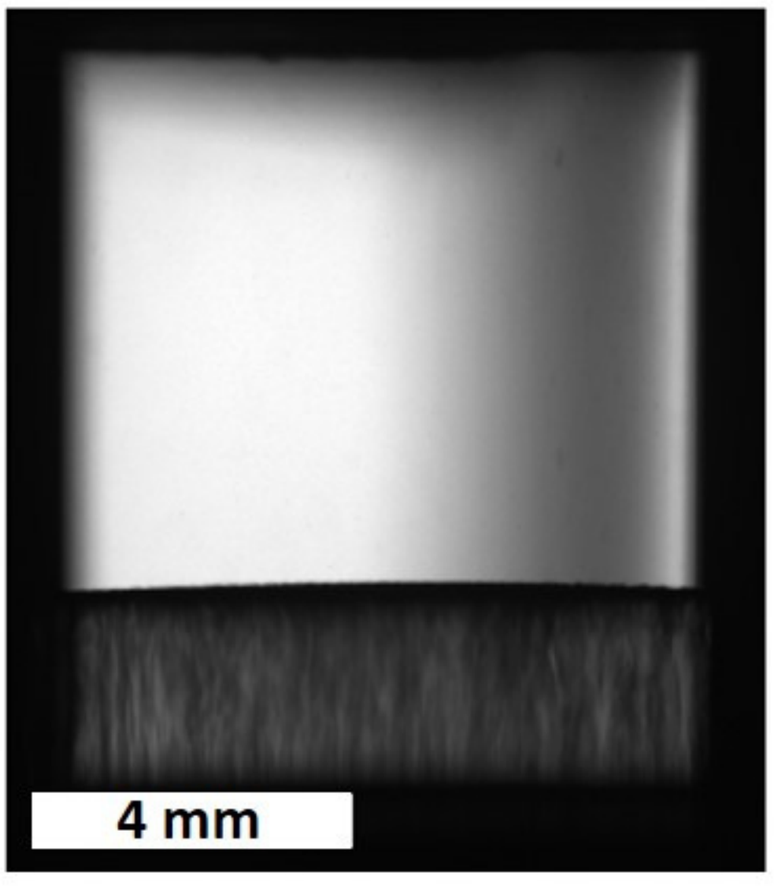
4 mm

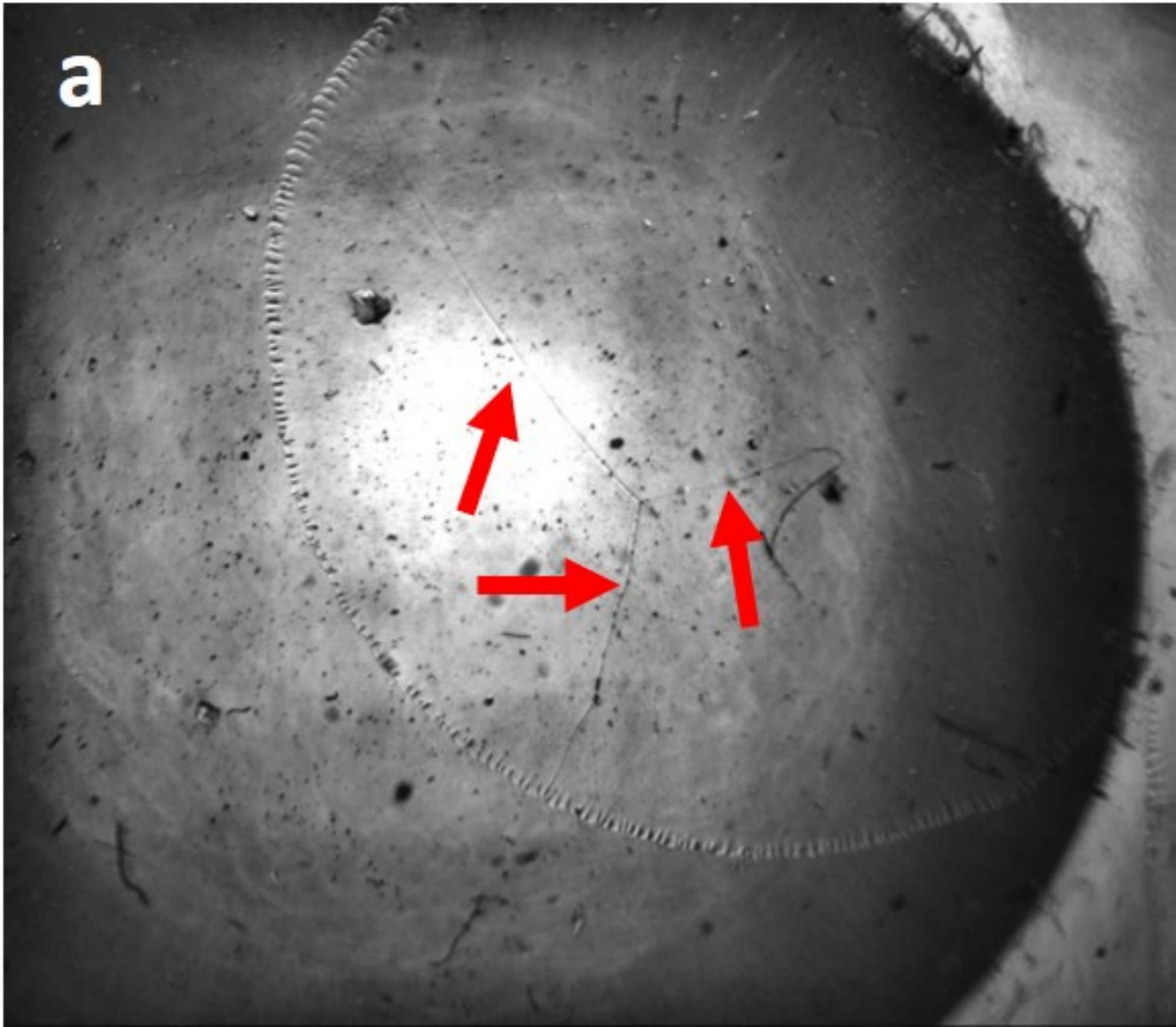
a

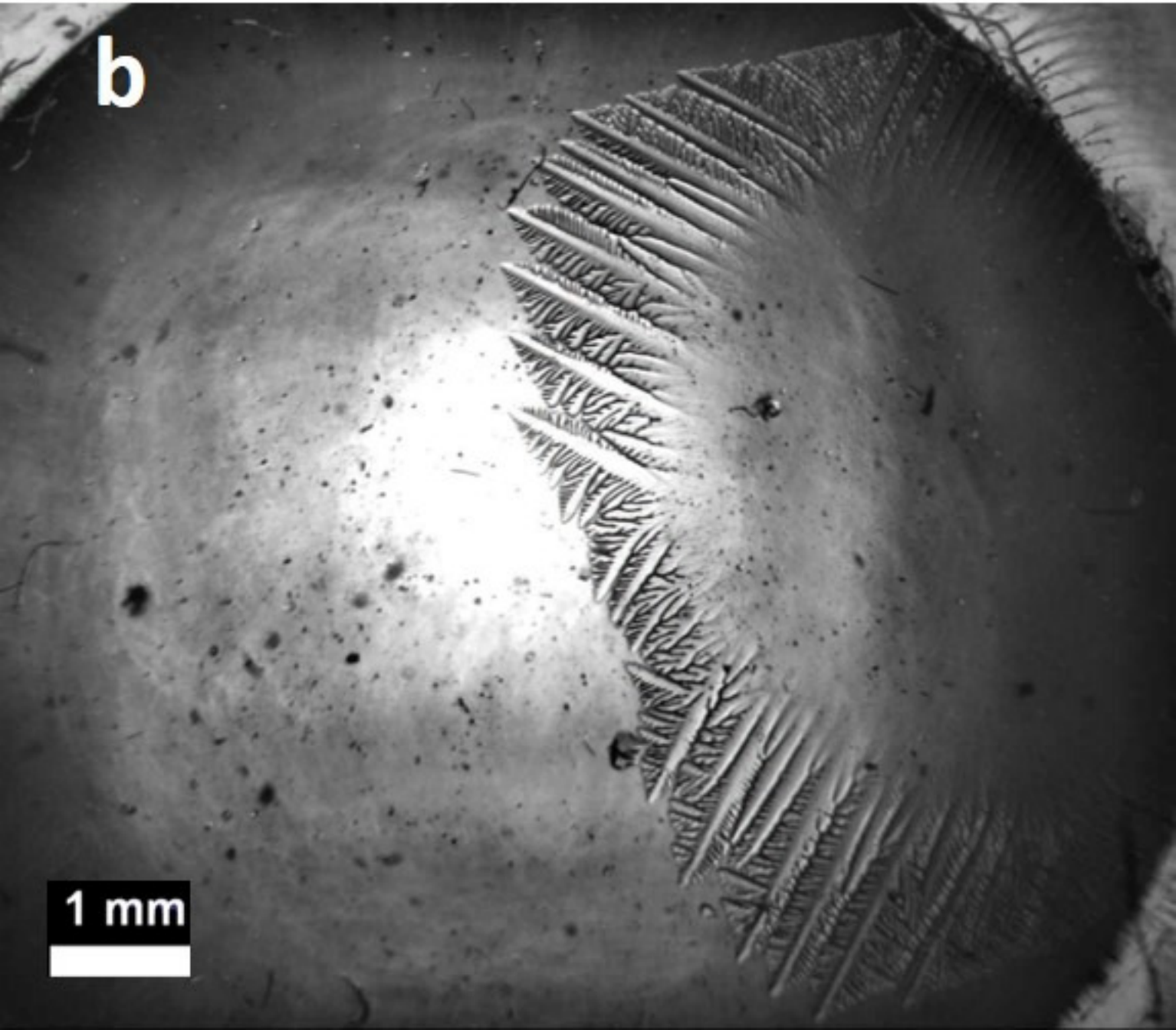
b
1 mm

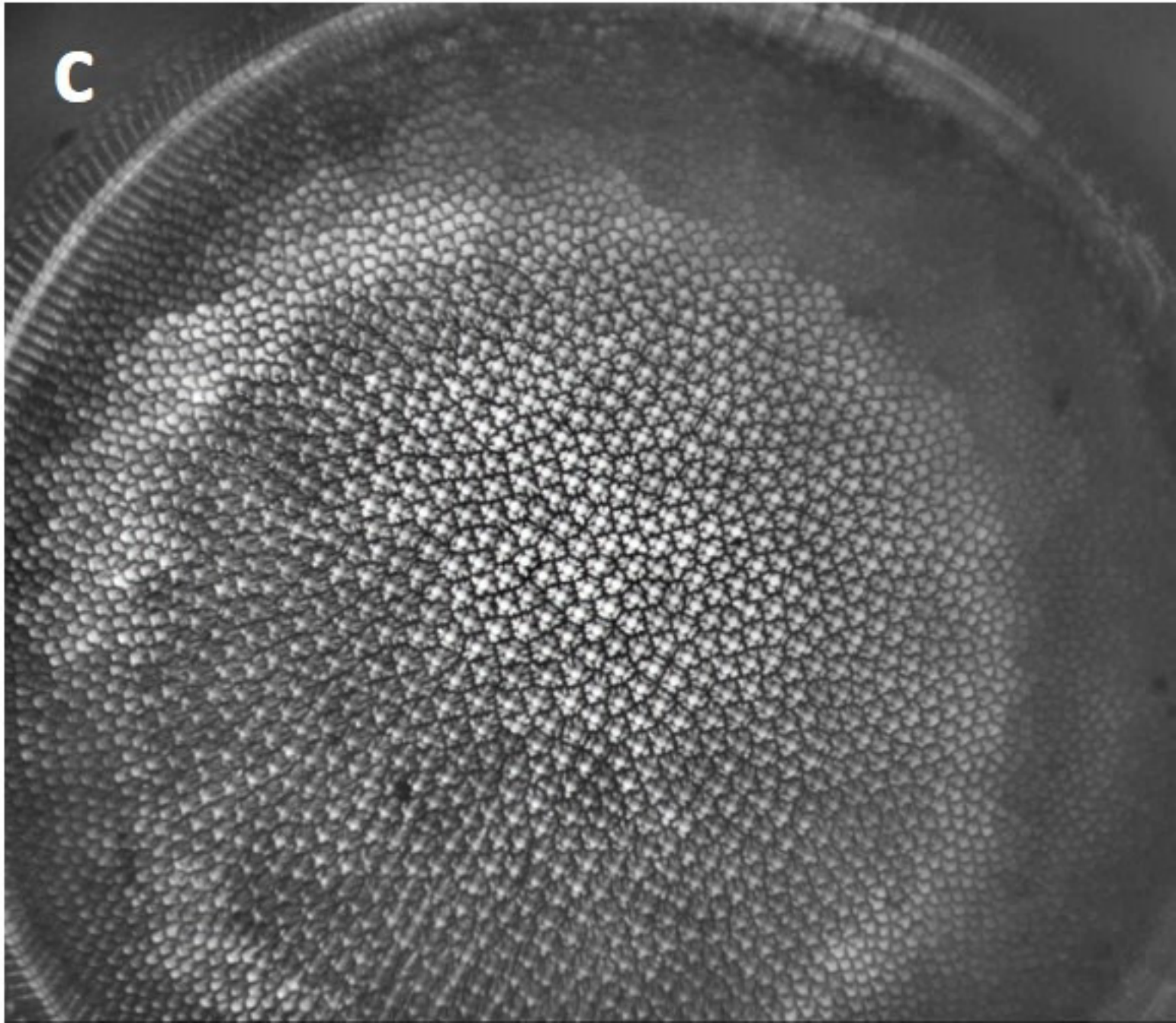
C

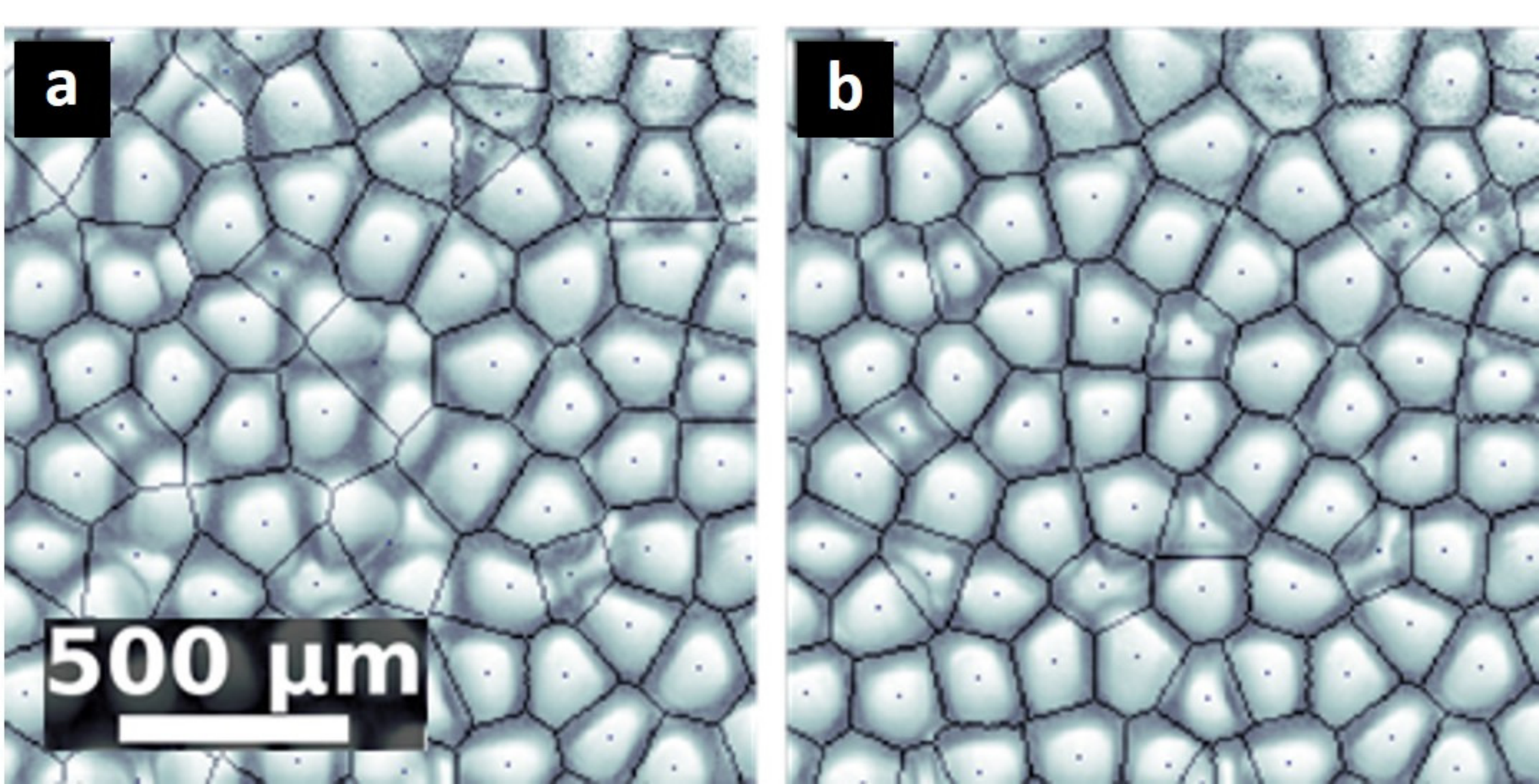
a
500 µm
b

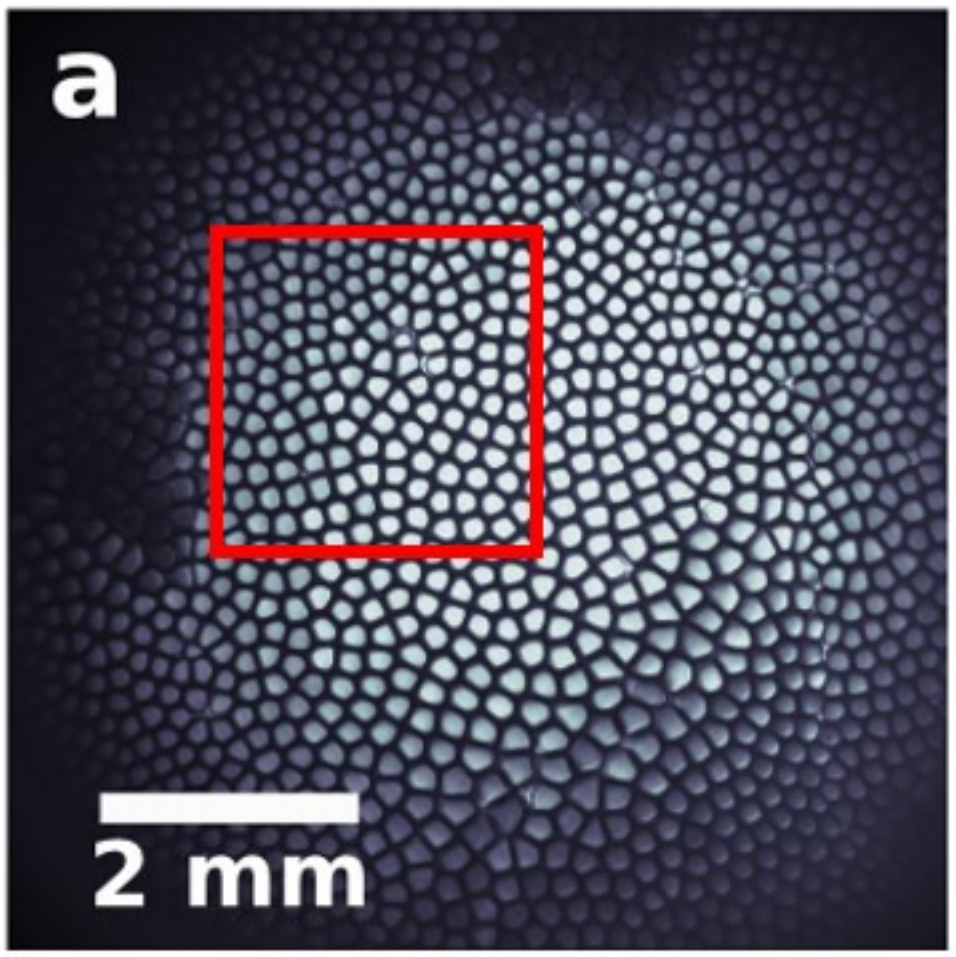
a
2 mm

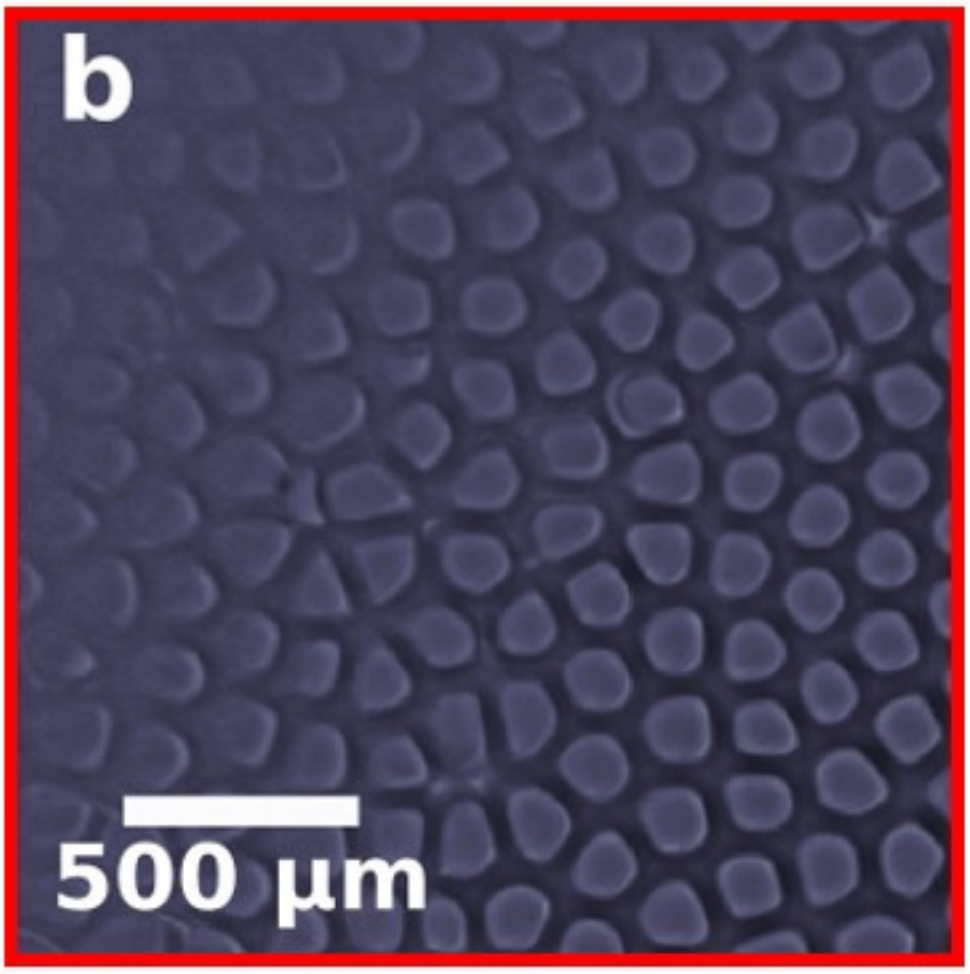
b
500 µm

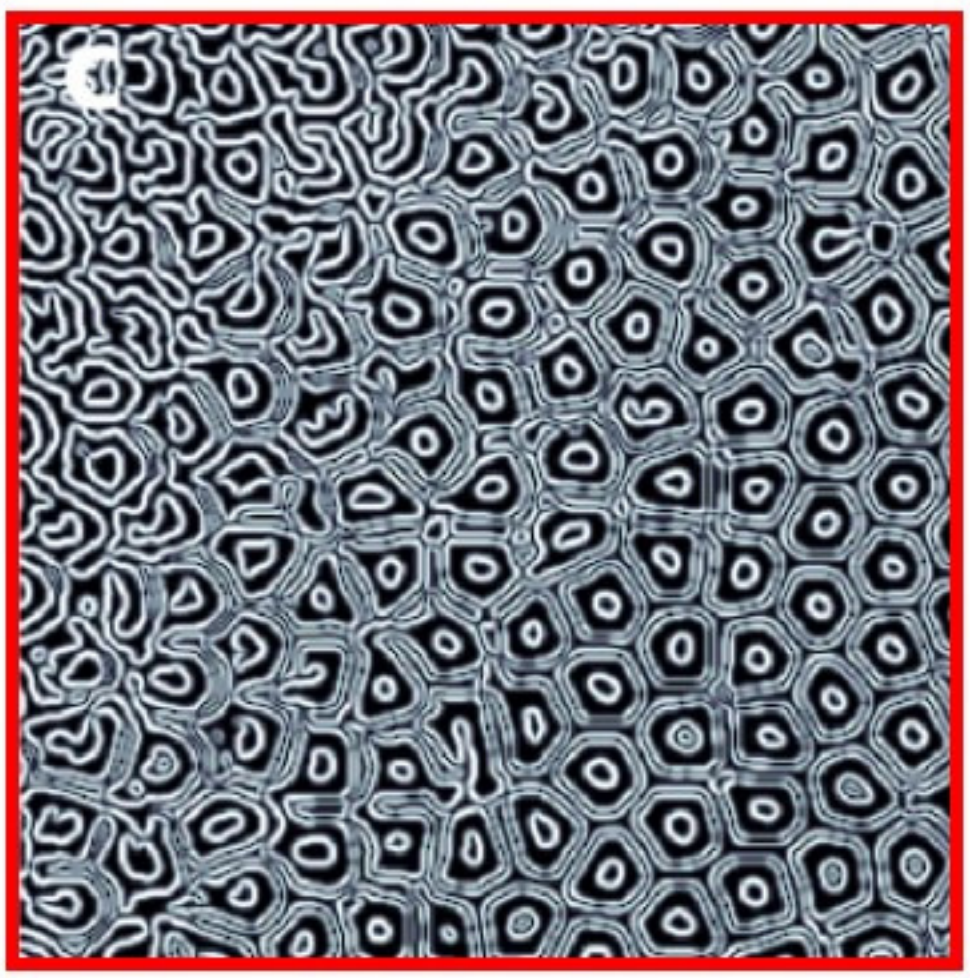
c

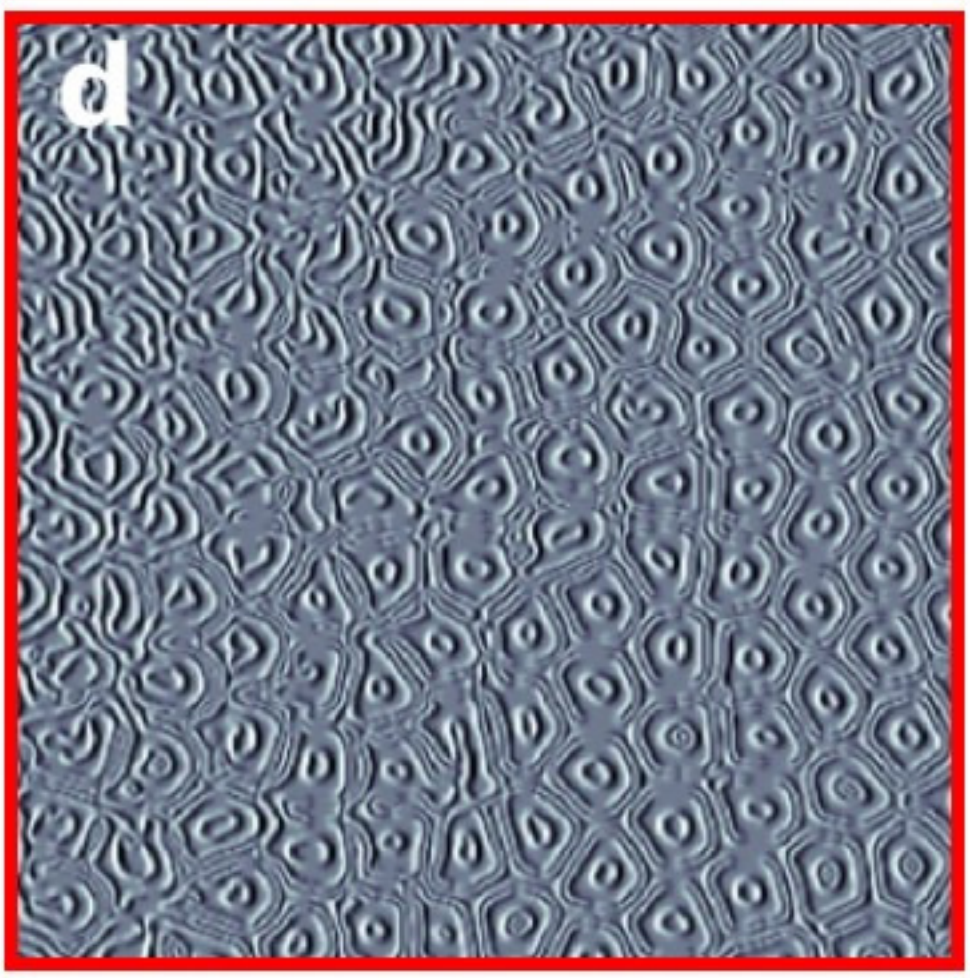
d

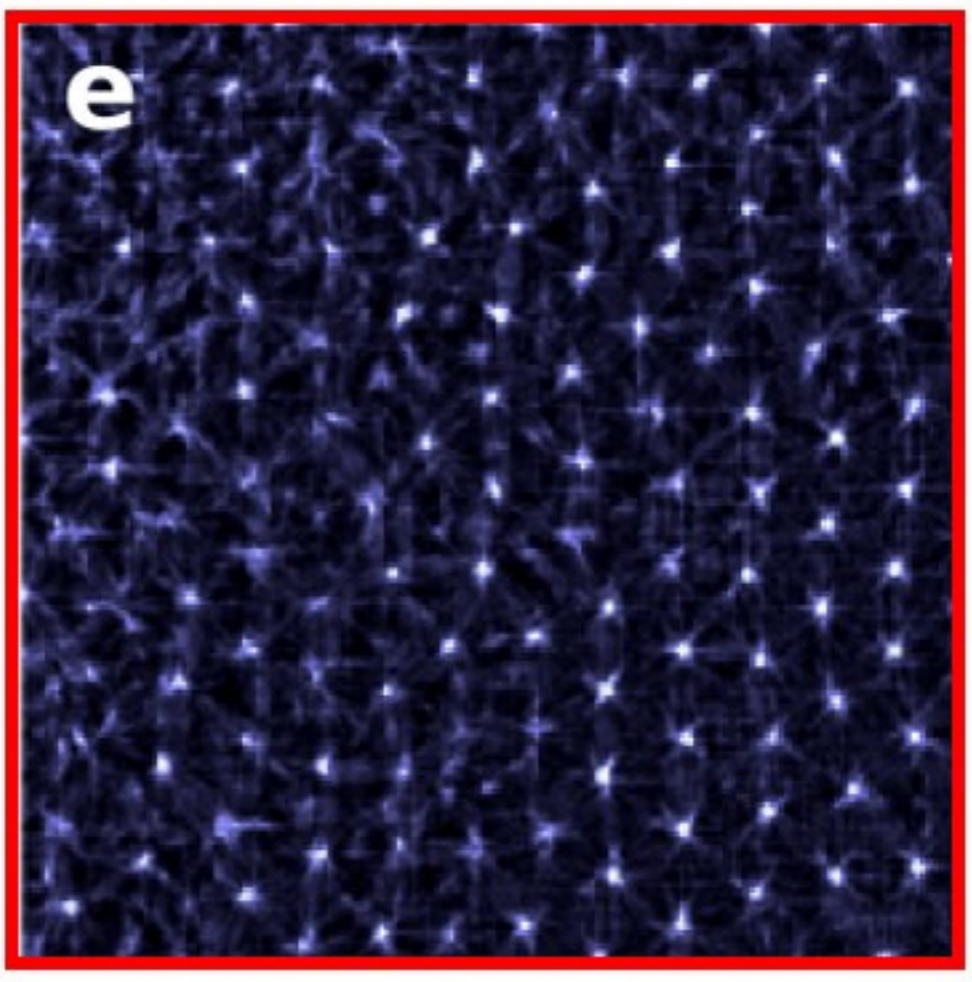
e

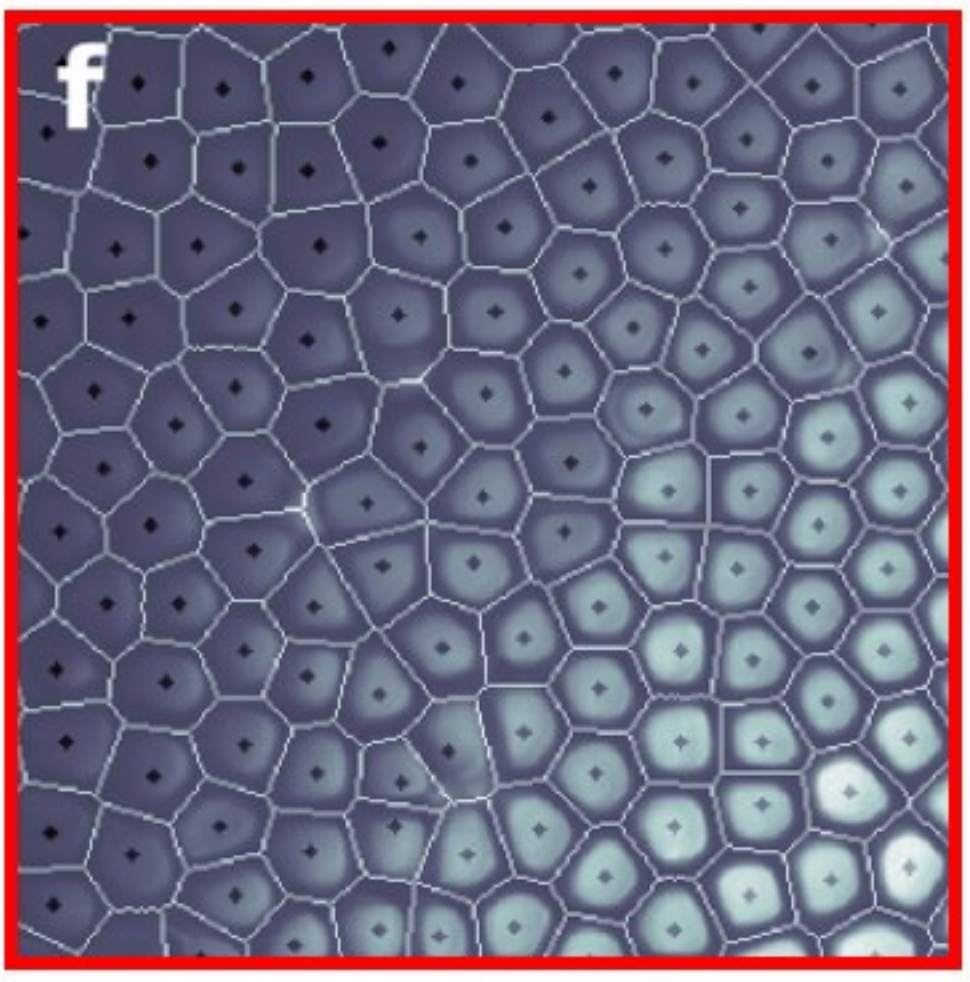
f

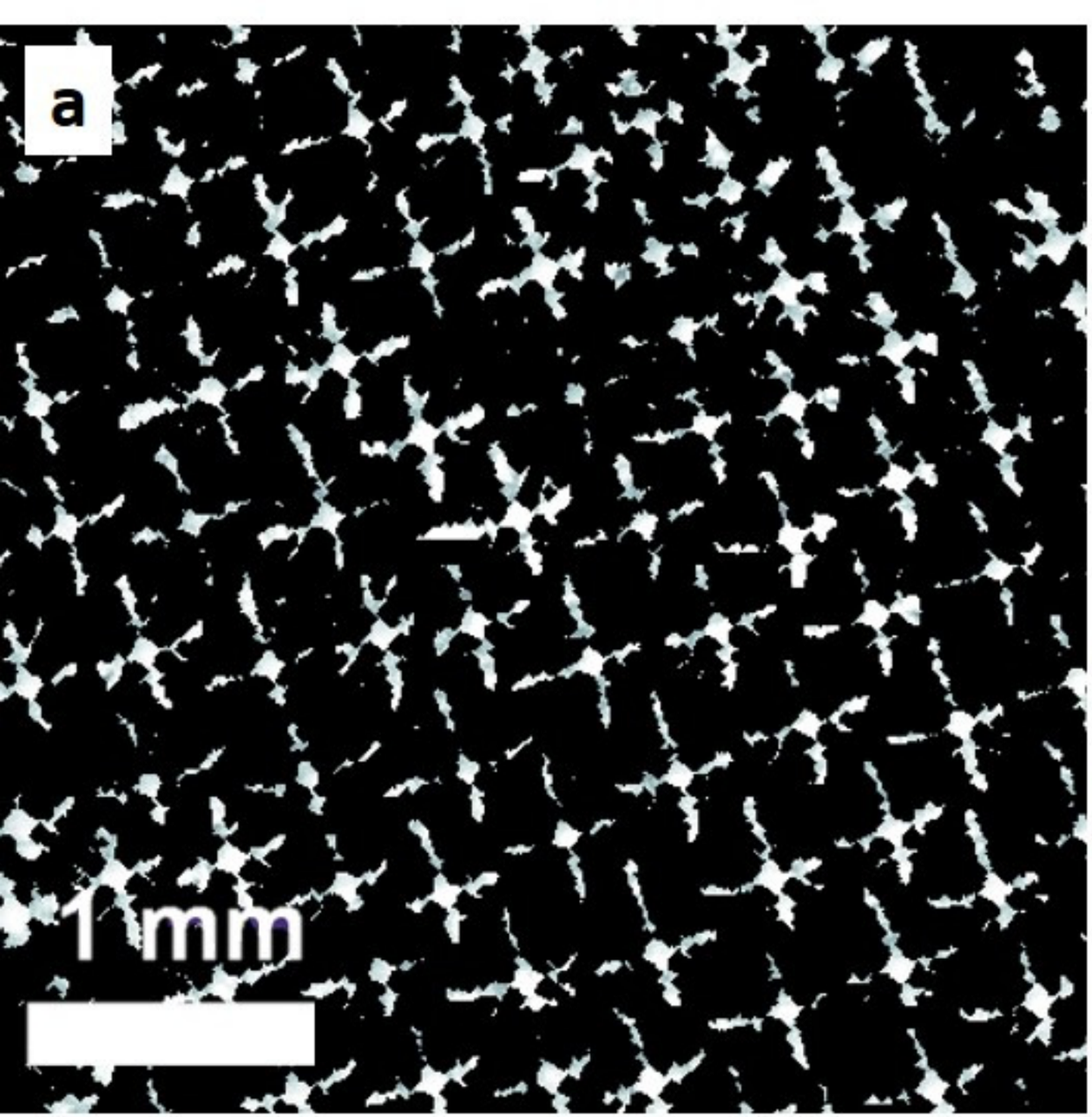
a
1 mm

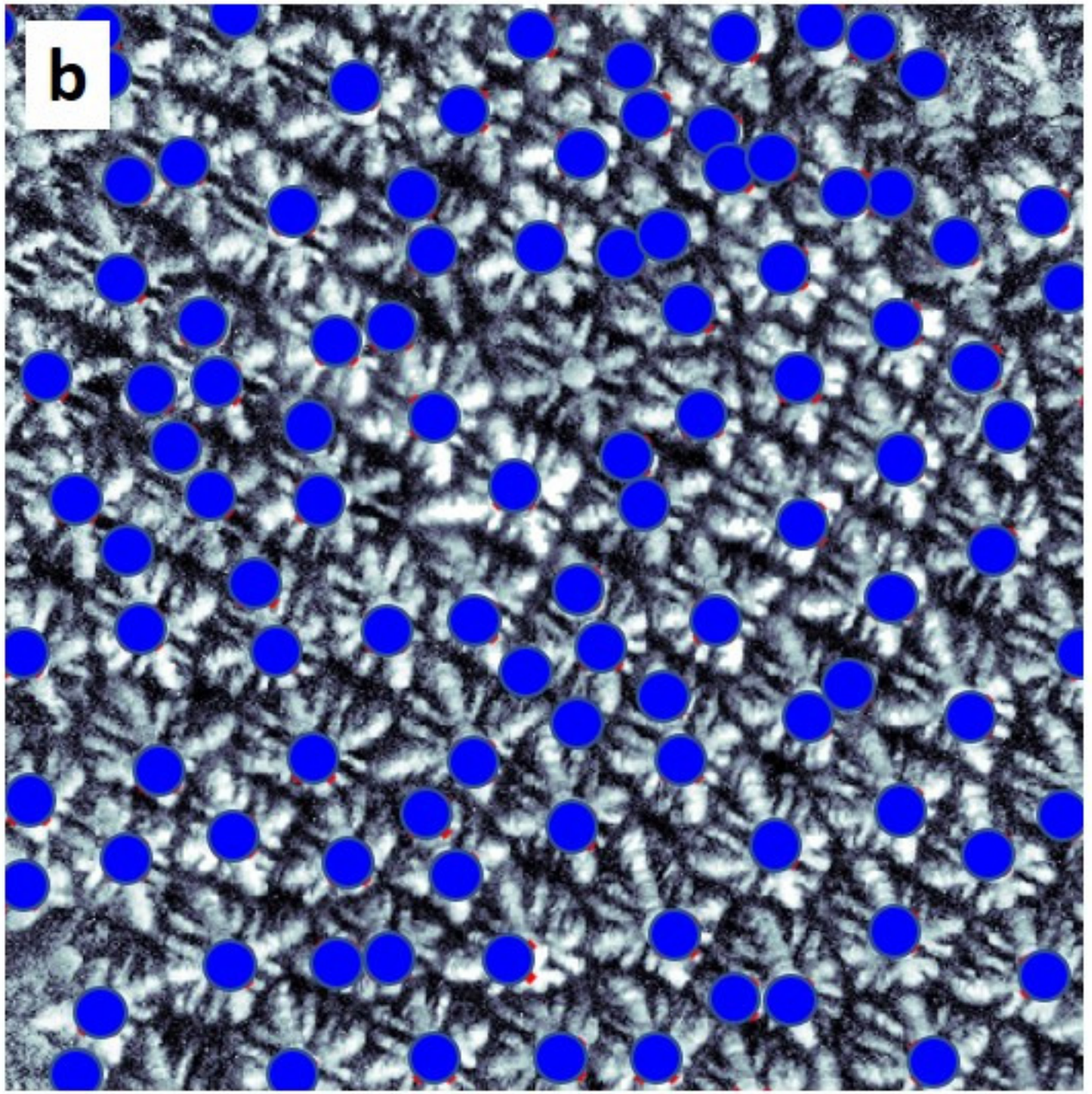
b

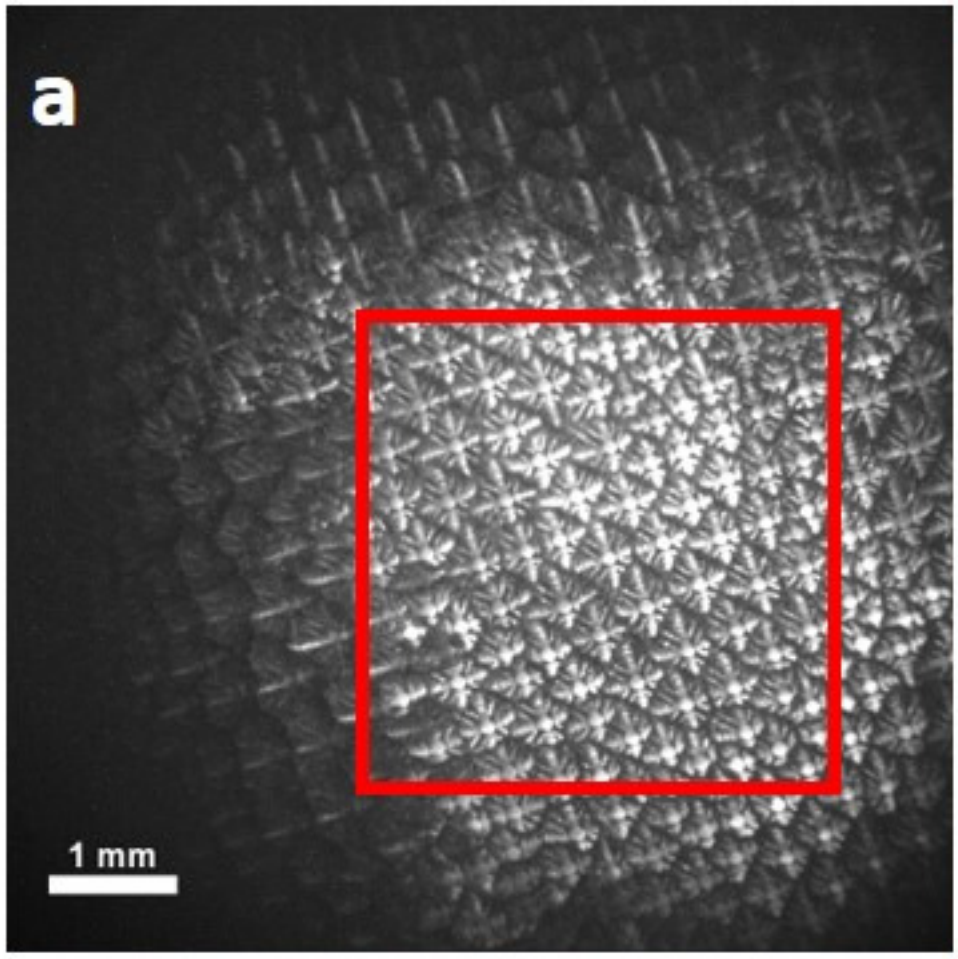
a
1 mm

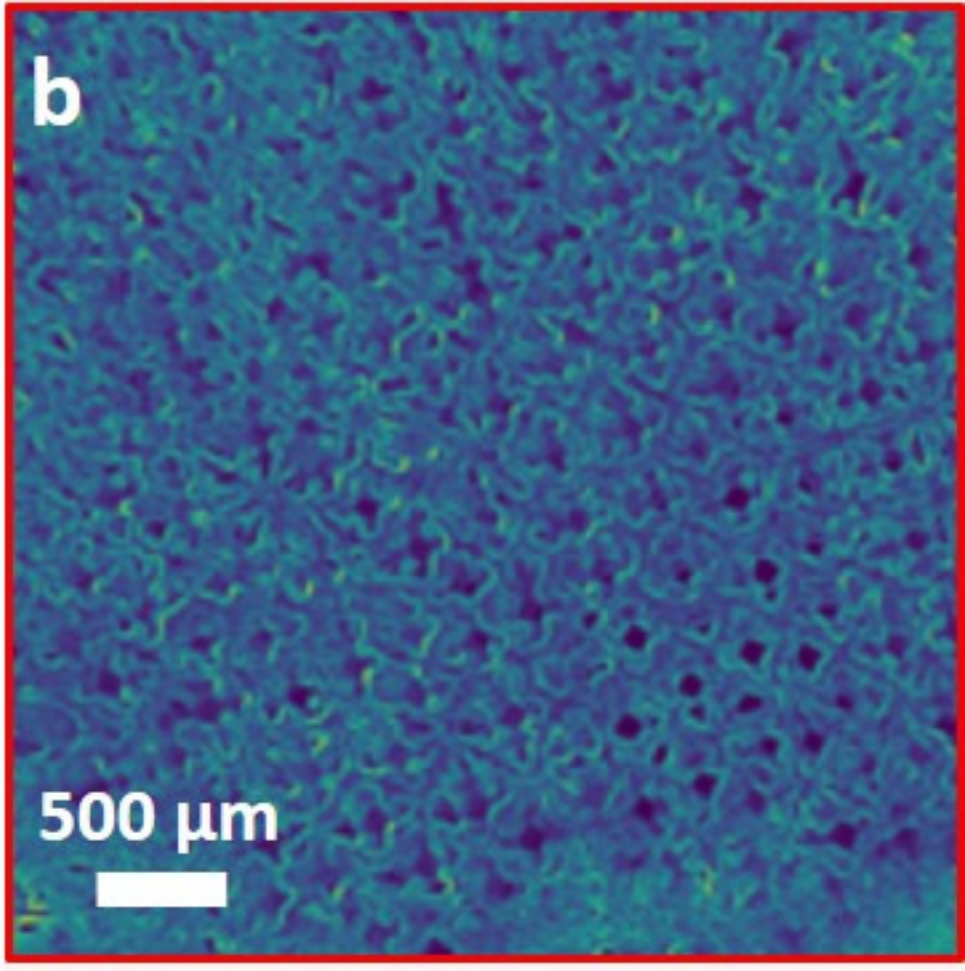
b
500 µm

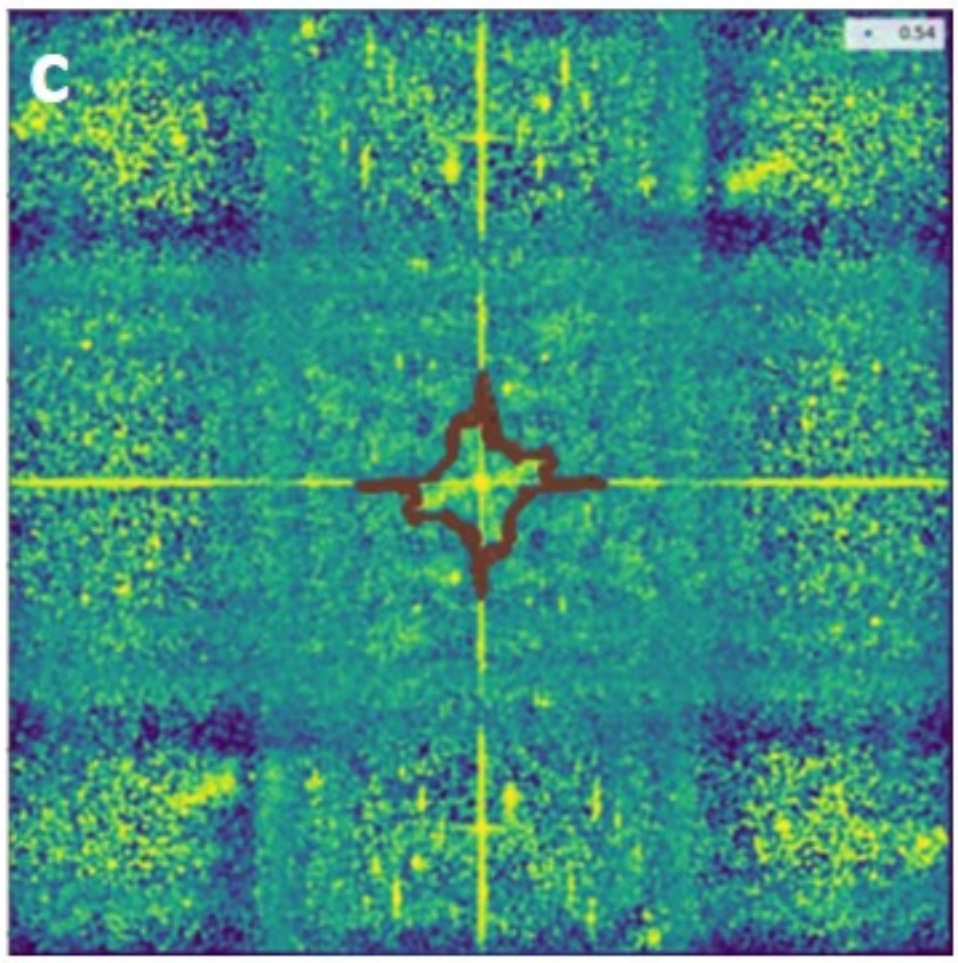
c

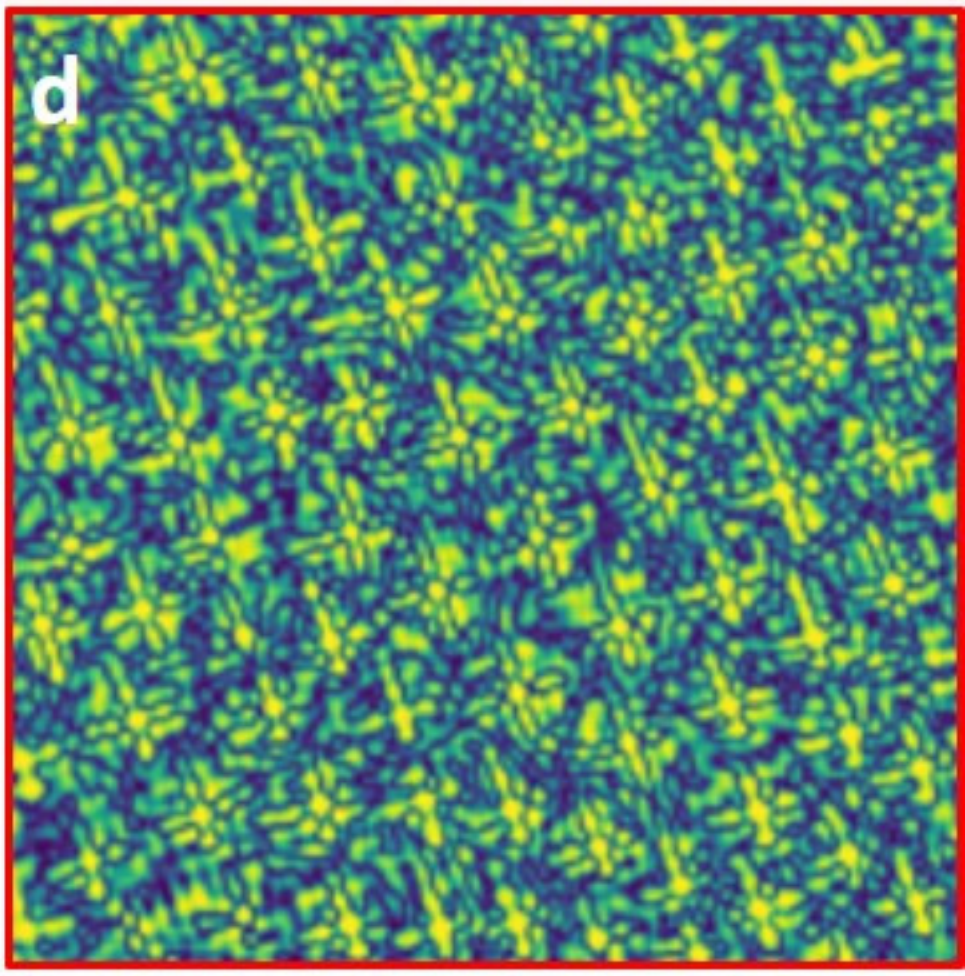
d

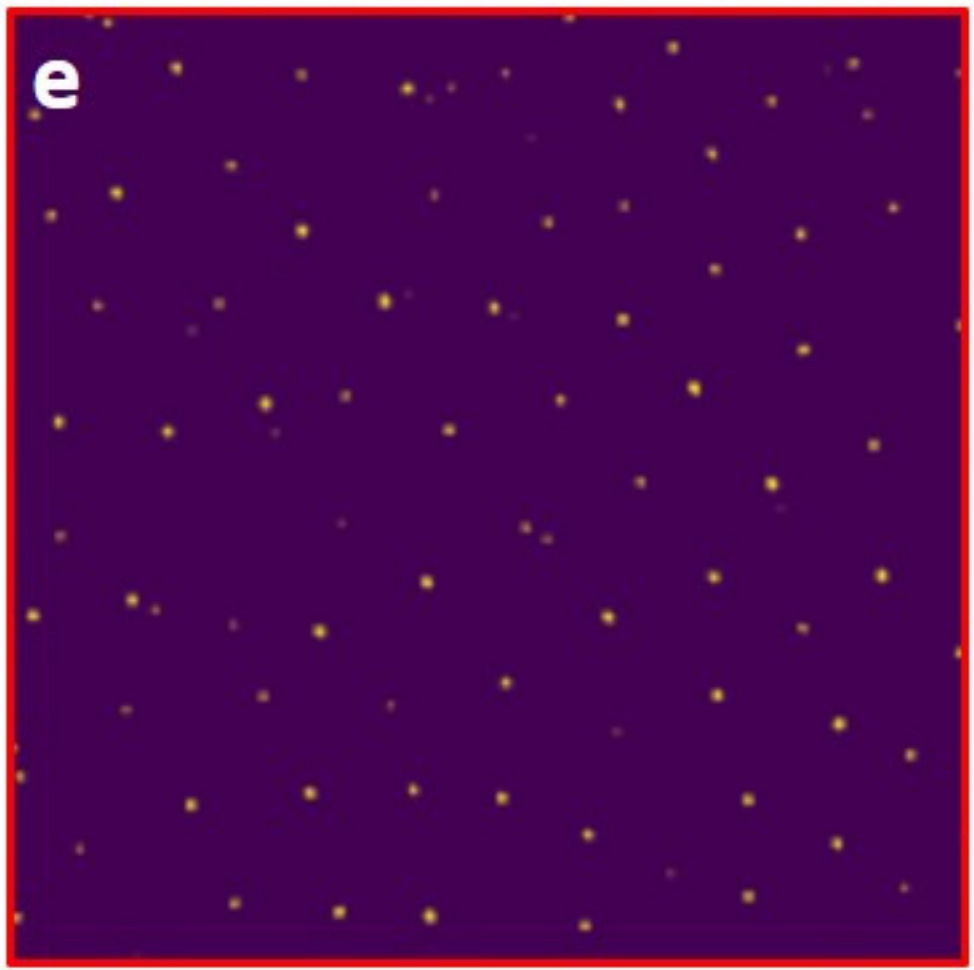
e

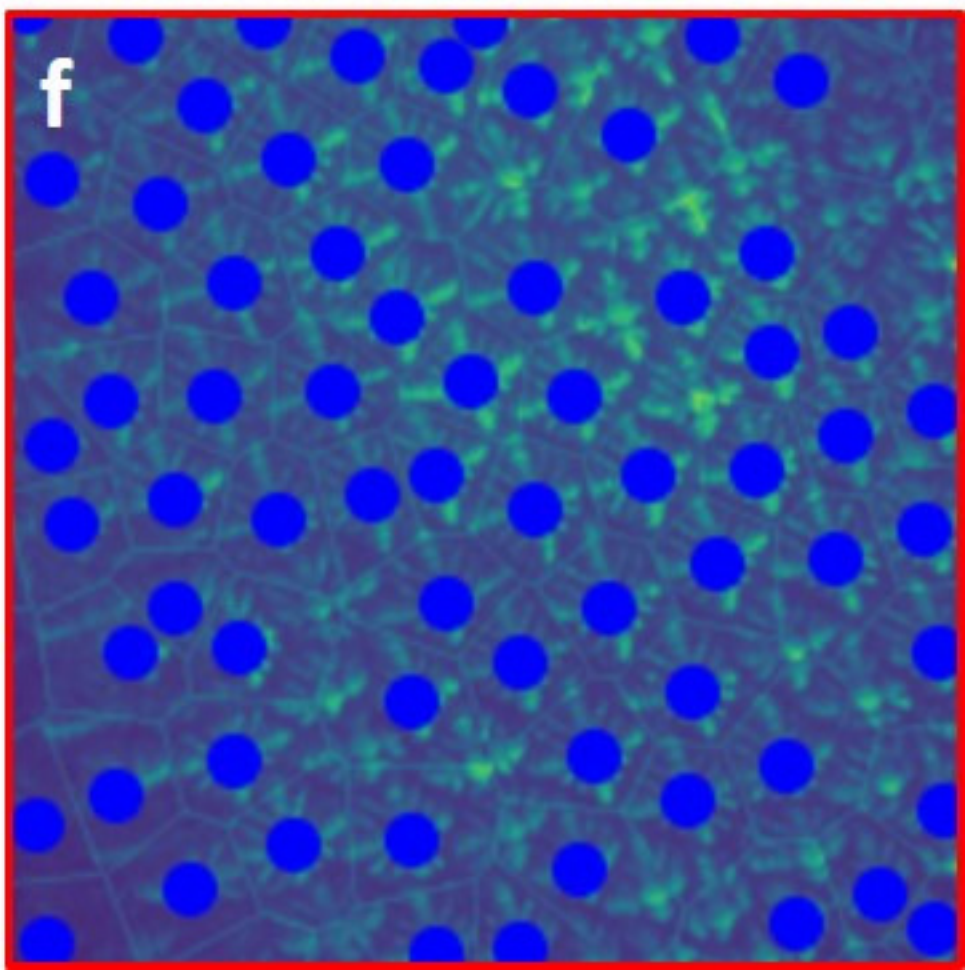
f

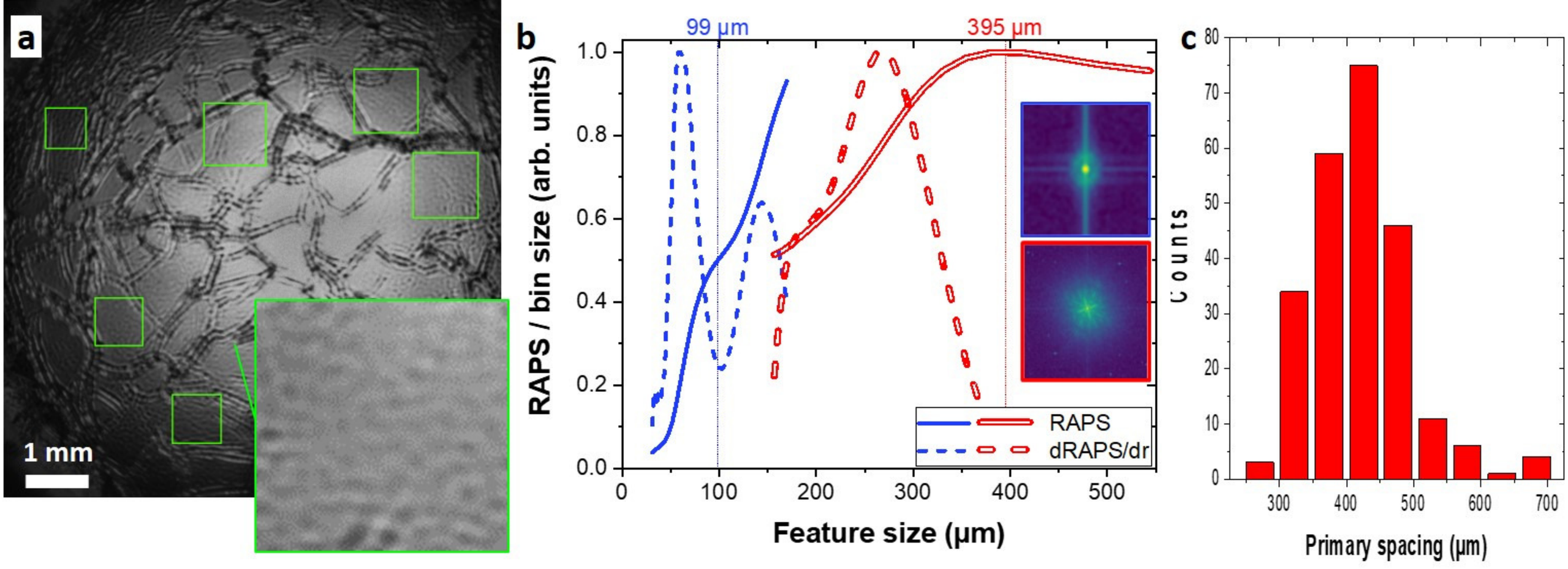
a
1 mm
b
99 µm
395 µm
RAPS / bin size (arb. units)
Feature size (µm)
RAPS
dRAPS/dr
c
Counts
Primary spacing (µm)

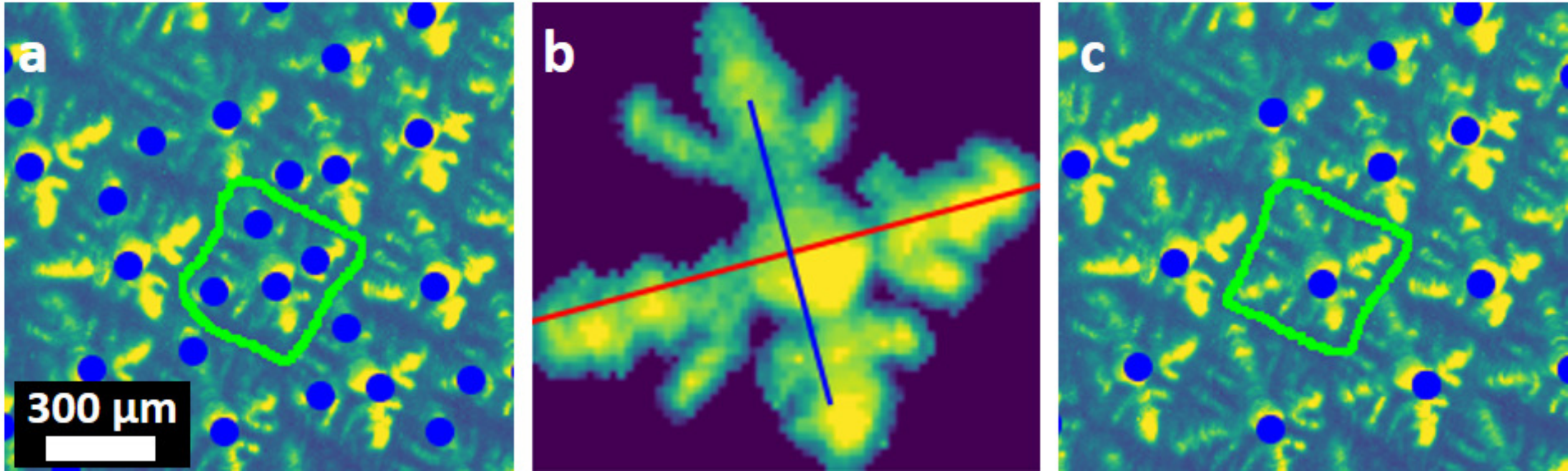
a
b
c
300 µm

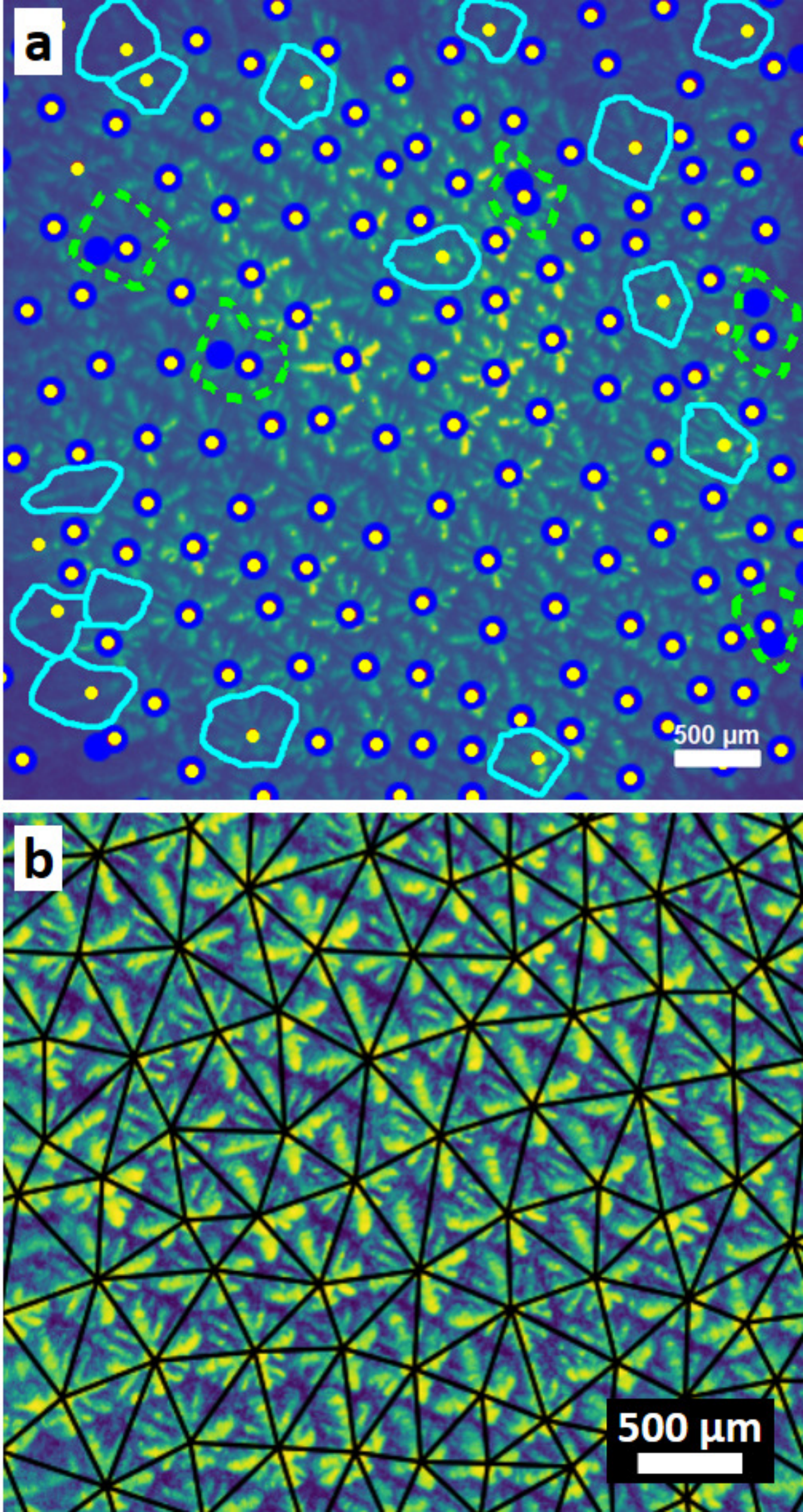
a
500 µm
b
500 µm

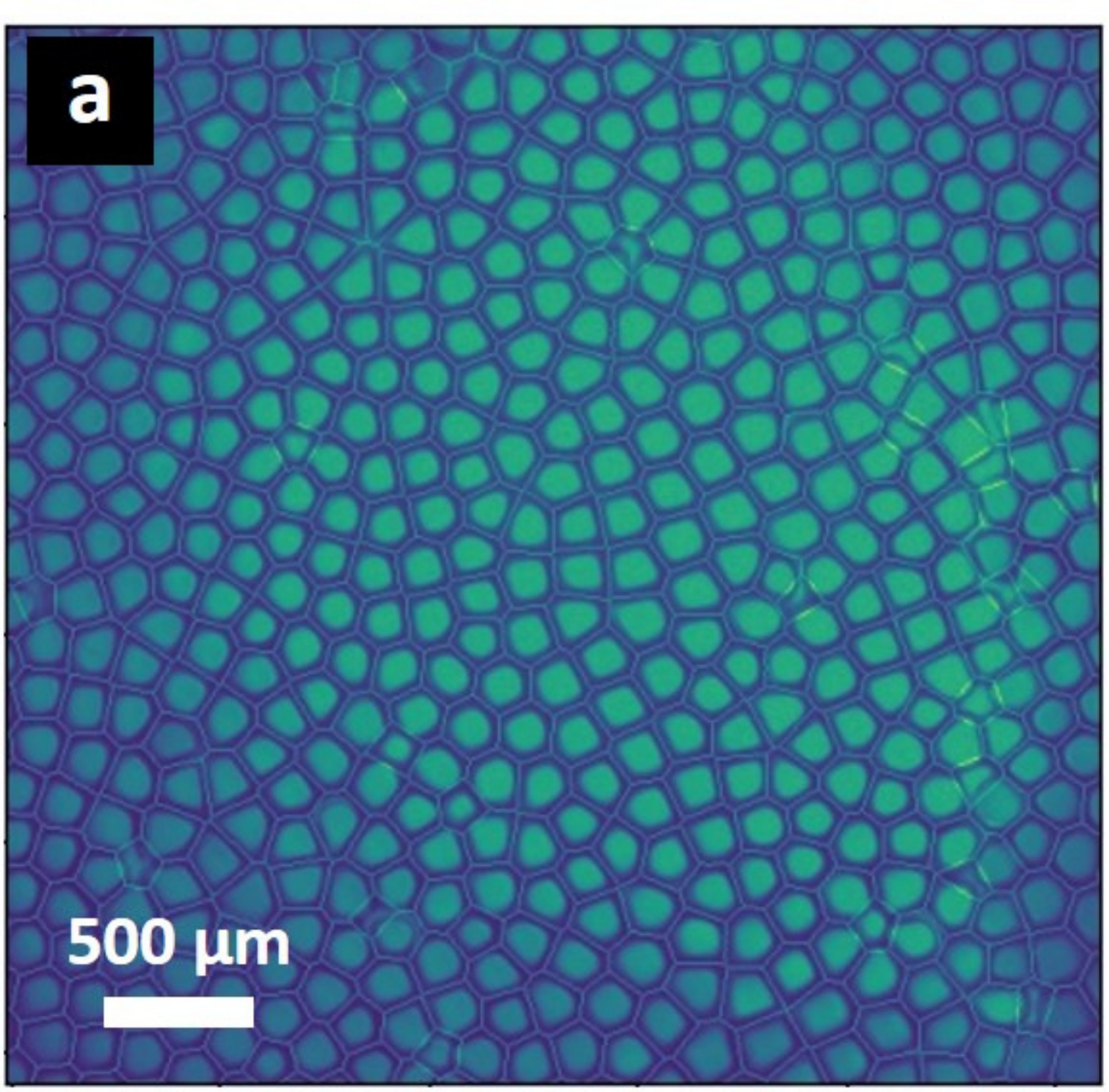
a
500 µm

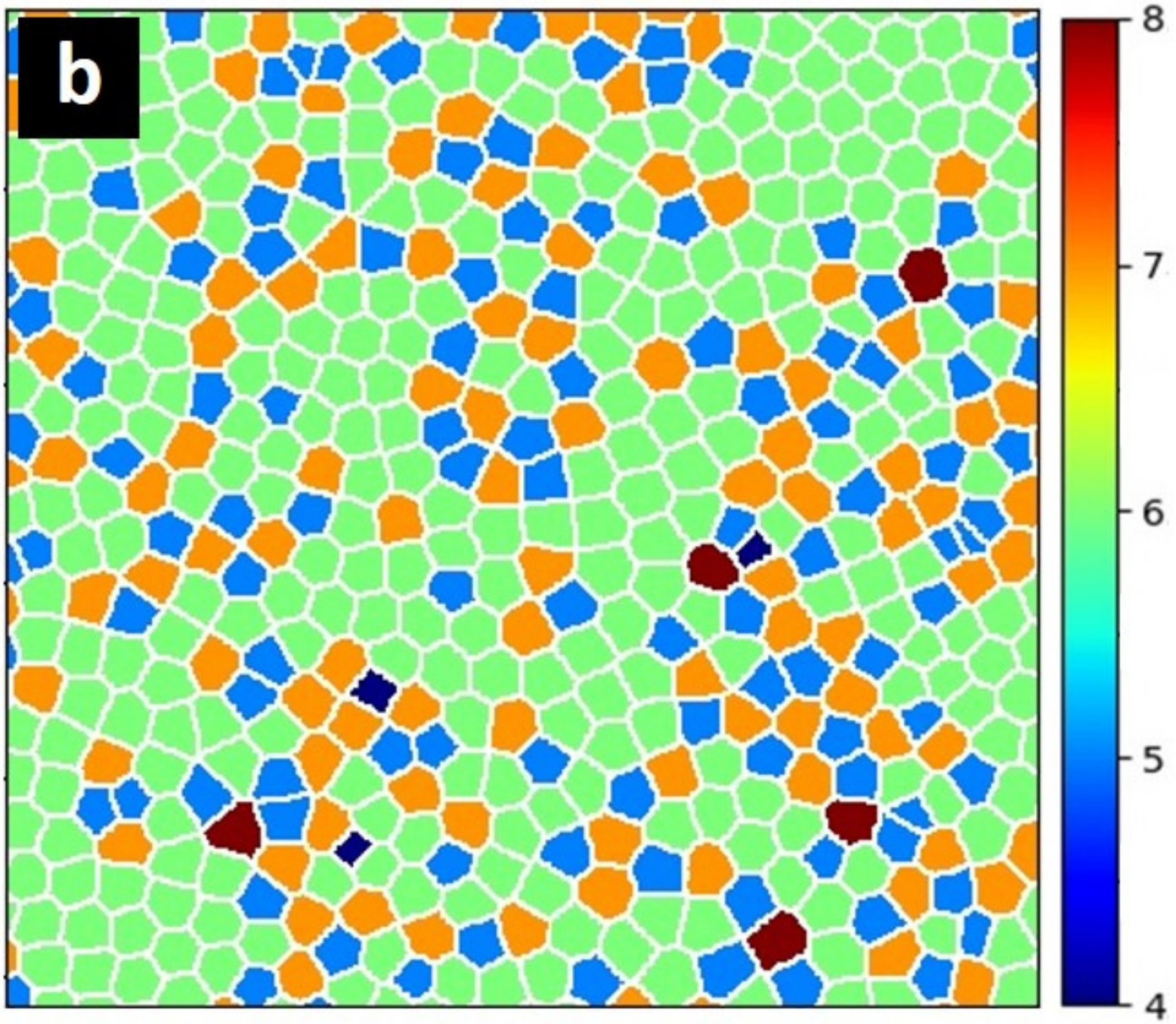
b
8
7
6
5
4

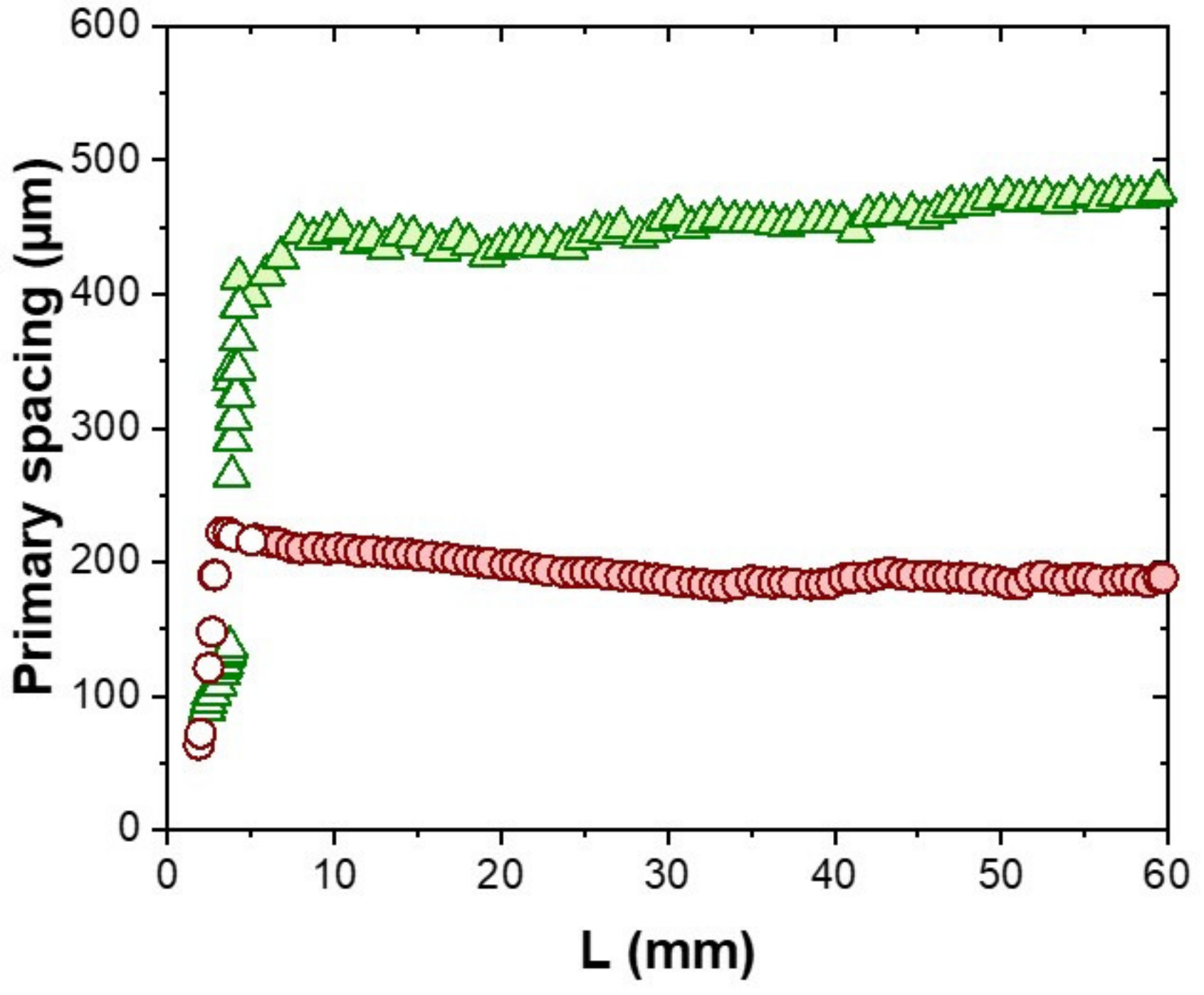
Primary spacing (μm)
L (mm)
0
100
200
300
400
500
600
0
10
20
30
40
50
60

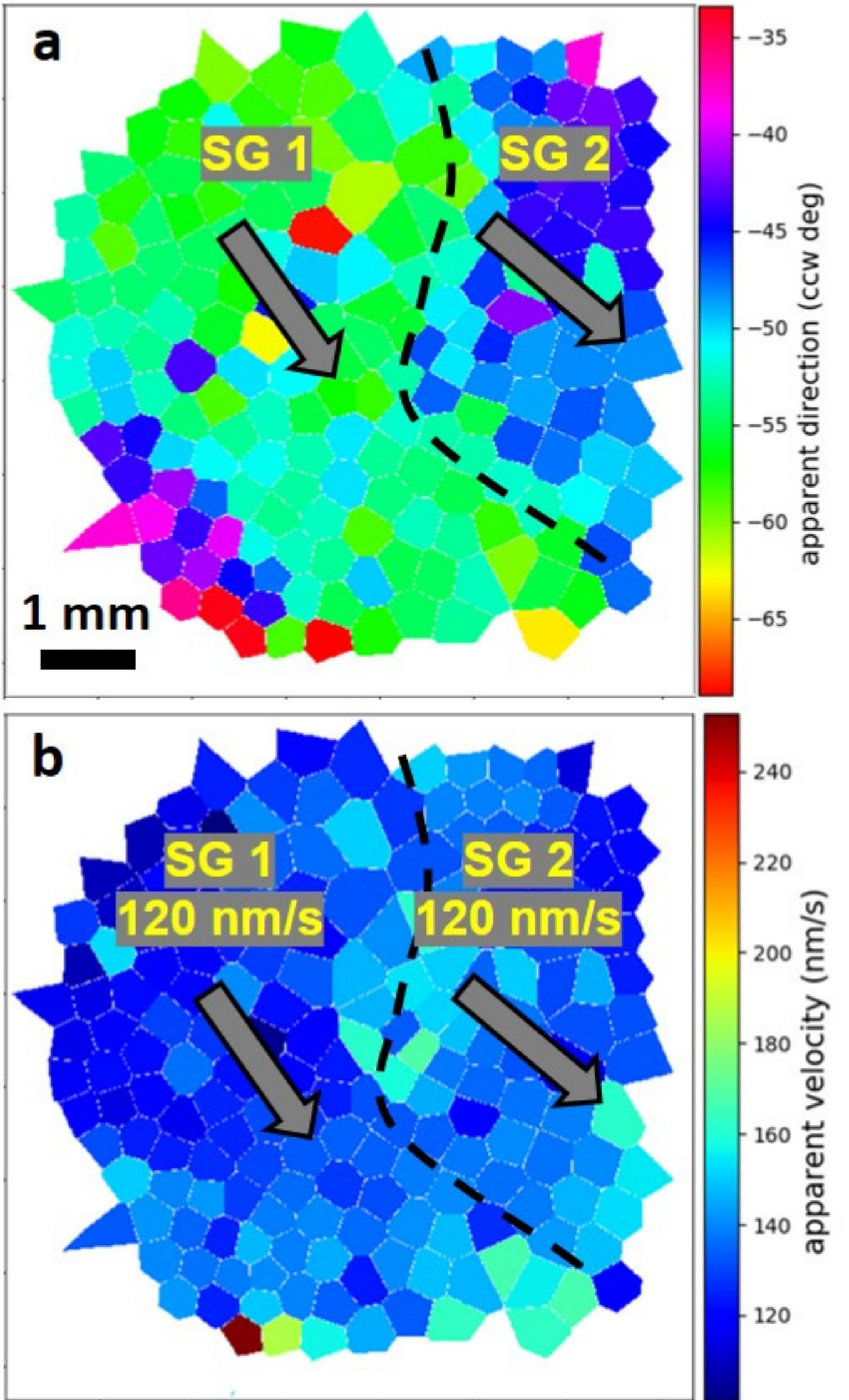
a
SG 1
SG 2
1 mm
−35
−40
−45
−50
−55
−60
−65
apparent direction (ccw deg)
b
SG 1
120 nm/s
SG 2
120 nm/s
240
220
200
180
160
140
120
apparent velocity (nm/s)

a

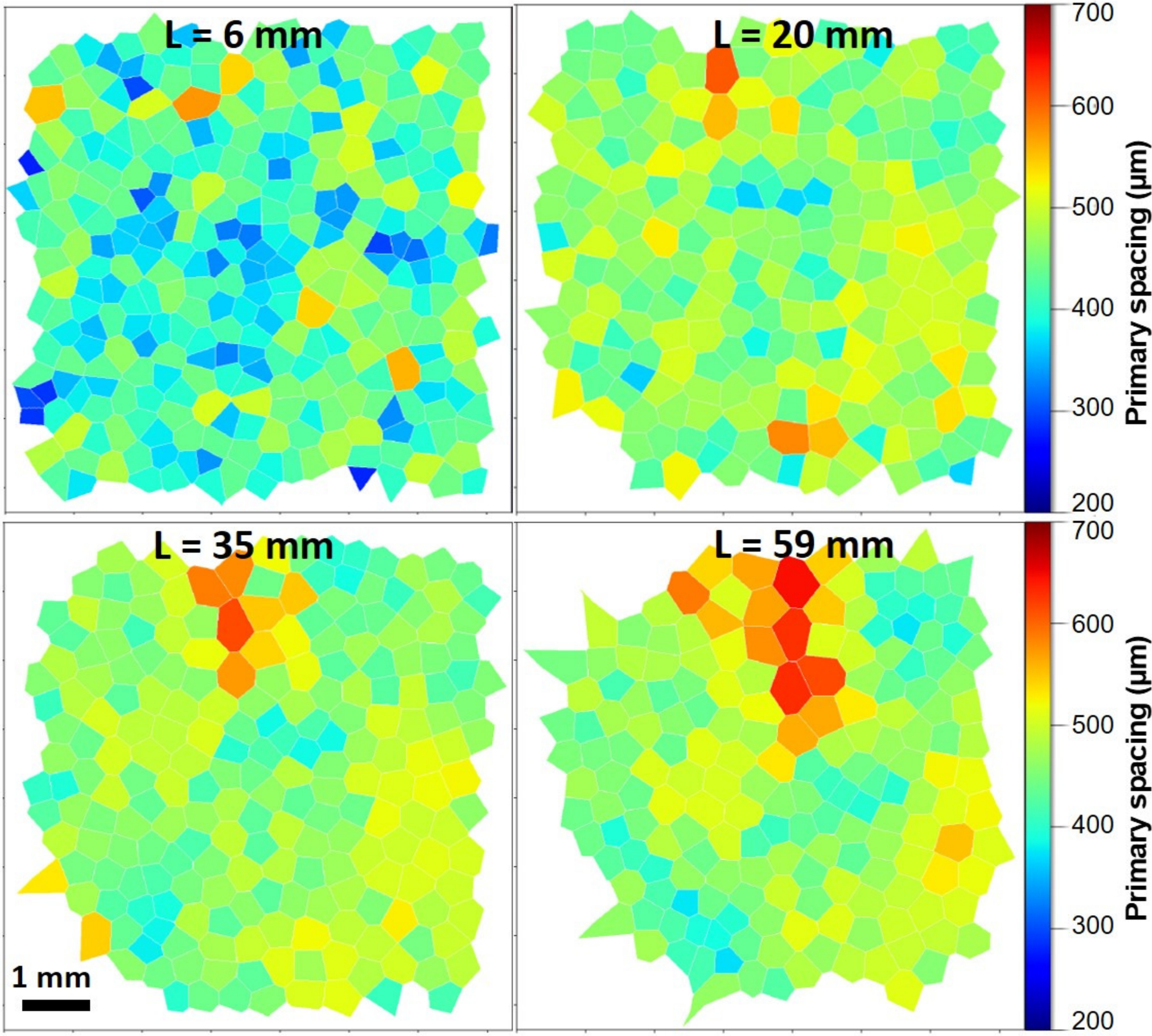
L = 6 mm
L = 20 mm
L = 35 mm
L = 59 mm
1 mm
700
600
500
400
300
200
Primary spacing (μm)

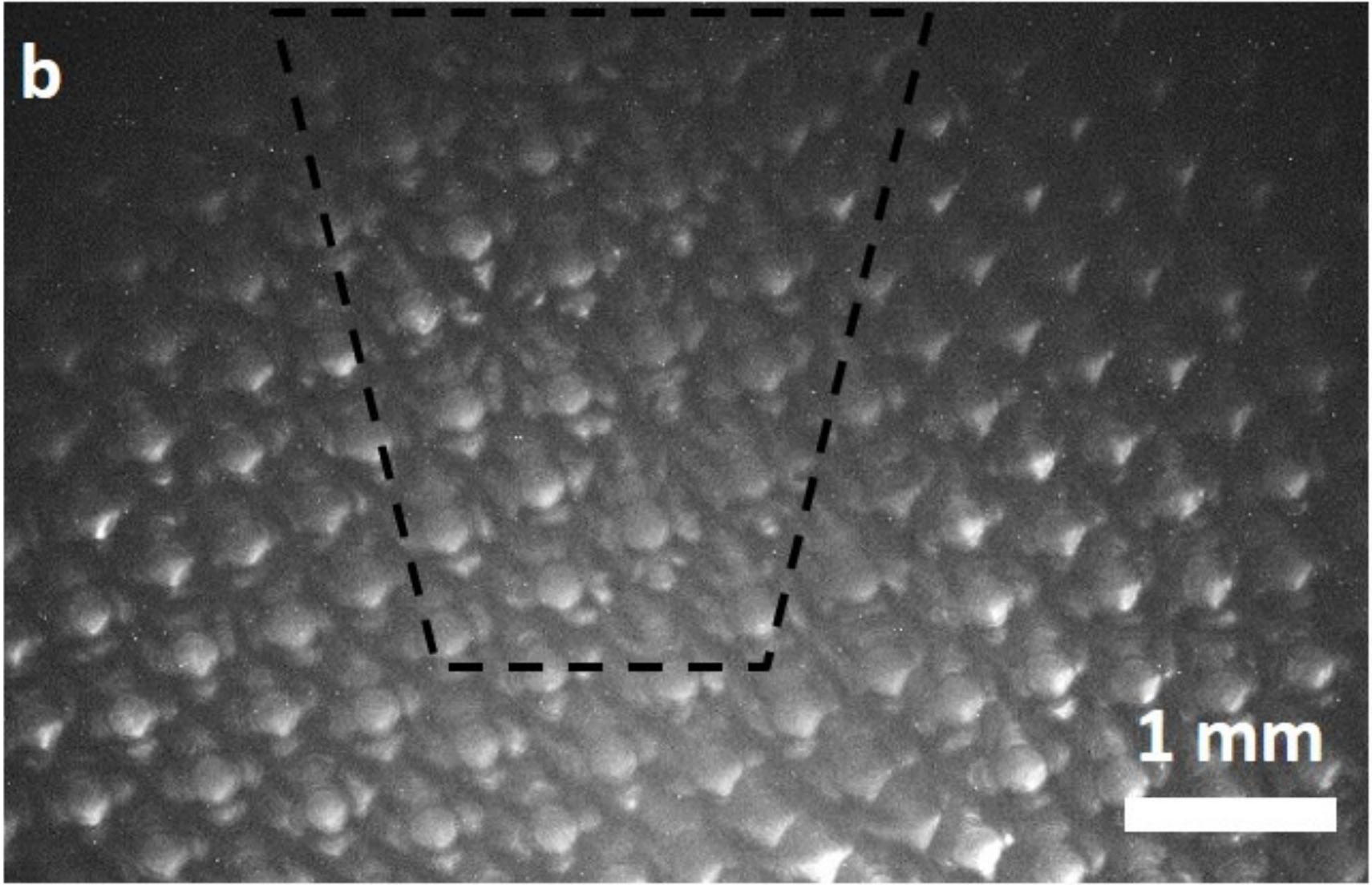
b
1 mm